Nucleic Acids Research, 2025, **53**, gkaf521
https://doi.org/10.1093/nar/gkaf521
Molecular and Structural Biology

DnaB and DciA: mechanisms of helicase loading and translocation on ssDNA

Nicholas Gao [1,2,3,†], Daniele Mazzoletti [4,†], Adele Peng [1], Paul Dominic B Olinares [5], Castrese Morrone [4,6], Andrea Garavaglia [4,7], Nourelhoda Gouda [1], Sergey Tsoy [1], Albert Mendoza [1], Ahammad Chowdhury [1], Antonio Cerullo [1,8], Hrutvik Bhavsar [1], Franca Rossi [4], Menico Rizzi [4], Brian T. Chait [5], Riccardo Miggiano [4,*], David Jeruzalmi [1,2,8,9,*]

[1]Department of Chemistry and Biochemistry, City College of New York, New York, NY 10031, United States
[2]Ph.D. Program in Biochemistry, The Graduate Center of the City University of New York, New York, NY 10016, USA
[3]Present address: Nicholas Gao, Mirimus Inc., 760 Parkside Ave, Brooklyn, NY 11226, USA
[4]Department of Pharmaceutical Sciences, University of Piemonte Orientale, Novara 28100, Italy
[5]Laboratory for Mass Spectrometry and Gaseous Ion Chemistry, The Rockefeller University, New York, New York 10065, United States
[6]Present address: Castrese Morrone, Telethon Institute of Genetics and Medicine (TIGEM) Via Campi Flegrei, 34 80078 Pozzuoli (NA), Italy
[7]Present address: Andrea Garavaglia, Department of Pharmaceutical Science (DISFARM), University of Milan, Milan 20133, Italy
[8]Ph. D. Program in Chemistry, The Graduate Center of the City University of New York, New York, NY 10016, USA
[9]Ph. D. Program in Biology, The Graduate Center of the City University of New York, New York, NY 10016, USA

[*]To whom correspondence should be addressed. Email: dj@ccny.cuny.edu
Correspondence may also be addressed to Riccardo Miggiano. Email: riccardo.miggiano@uniupo.it
[†]These authors contributed equally.

Abstract

Replicative helicases are assembled on chromosomes by helicase loaders before the initiation of DNA replication. Here, we investigate the mechanisms employed by the bacterial *Vibrio cholerae* (*Vc*) DnaB replicative helicase and the DciA helicase loader. Structural analysis of the ATPγS form of the *Vc*DnaB–ssDNA complex reveals a configuration distinct from that observed with GDP•AlF_4. With ATPγS, the amino-terminal domain (NTD) tier, previously found as an open spiral in the GDP•AlF_4 complex, adopts a closed planar arrangement. Furthermore, the DnaB subunit at the top of the carboxy-terminal domain (CTD) spiral is displaced by approximately 25 Å between the two forms. We suggest that remodeling the NTD layer between closed planar and open spiral configurations, along with the migration of two distinct CTDs to the top of the DnaB spiral, repeated three times, mediates hand-over-hand translocation. Biochemical analysis indicates that *Vc*DciA utilizes its Lasso domain to interact with DnaB near its Docking–Helix Linker–Helix interface. Up to three copies of *Vc*DciA bind to *Vc*DnaB, suppressing its ATPase activity during loading onto physiological DNA substrates. Our data suggest that DciA loads DnaB onto DNA using the ring-opening mechanism.

Graphical abstract

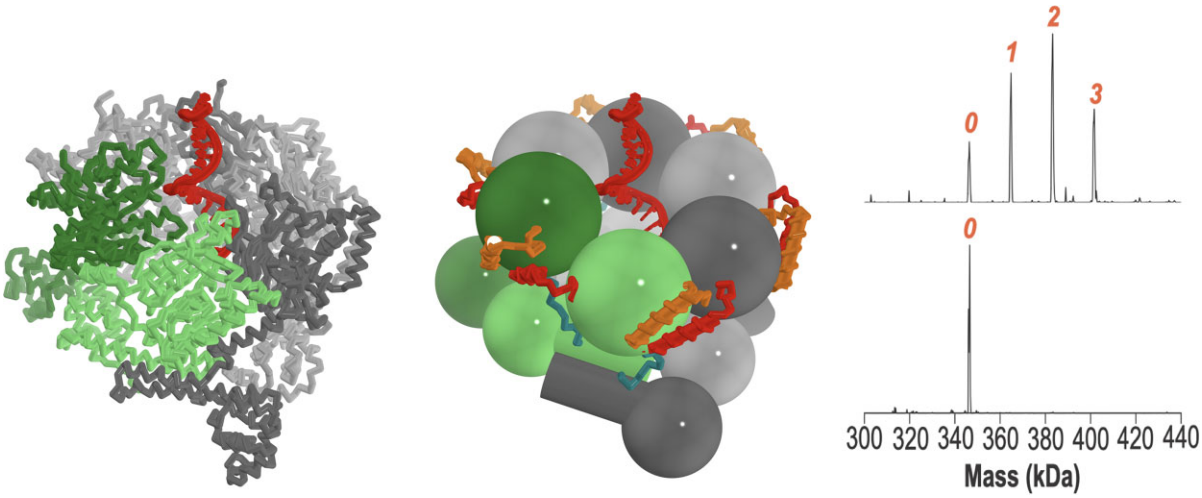

Received: October 2, 2024. **Revised:** May 24, 2025. **Editorial Decision:** May 27, 2025. **Accepted:** June 27, 2025

Introduction

Replisomes in all domains of life rely on replicative helicases to melt chromosomal DNA into single-stranded templates for DNA replication (Fig. 1) [1–6]. In *Escherichia coli*, the hexameric DnaB replicative helicase is a closed protein ring that encircles and translocates on one strand of DNA, excluding the second, as it prepares templates for DNA synthesis (Fig. 1). Members of the DnaB family [7–20] (henceforth: DnaB) and (reviewed in [21–27]) feature a two-tiered architecture, termed the amino-terminal domain (NTD) and the carboxy-terminal domain (CTD); each tier circumscribes a central channel through which ssDNA will traverse. A short linker helix (LH) connects each NTD and CTD; the LH packs against a neighboring CTD's docking helix (DH) in the complete hexamer. The translocating form of DnaB adopts a right-handed closed-spiral configuration and is suggested to operate using a hand-over-hand mechanism. Translocation occurs in a manner akin to a human using two hands to climb a rope, except that DnaB has six hands [10]. ATP hydrolysis on a DnaB subunit at the bottom of the spiral (in the pose in Fig. 2A and B) initiates translocation. This subunit peels away from its DnaB partners and from ssDNA [10, 24, 28, 29], migrates to the top of the spiral, binds ATP, docks onto a DnaB subunit via its β-hairpin arginine finger, and binds ssDNA position 3′ from the original location. Translocation continues via additional subunit migrations from the bottom to the top of the DnaB spiral [10]. Crucial support for this model emerged from a series of structures of the DnaB-family helicase Gp4 from phage T7 [24, 29].

Assembly of DnaB on single-stranded DNA (ssDNA) requires distinct mechanisms and loading factors (Supplementary Fig. S1). The loading factors include *E. coli* DnaC [30], bacteriophage λP [31], bacteriophage SPP1 G39P [32, 33], *Bacillus subtilis* (*Bst*) DnaI [34], T4 gene 59 [35], and phage P2 B [36]. Surprisingly, the genomes of most bacteria lack these well-studied loaders. Instead, most bacteria employ the structurally and possibly mechanistically distinct DciA or DopE family members [37–41]. Although the amino acid sequences of bacterial helicase loaders diverge significantly, they appear to mediate conserved mechanisms during helicase loading [11, 12, 14, 16, 19, 36, 42–48]. Loaders exhibit a conserved overall architecture, comprising a globular domain adjacent to an intrinsically disordered segment that often features an alpha helix at one or both termini, referred to as the lasso or grappling hook. Related arrangements can also be inferred for *Bacillus stearothermophilus* (*Bst*) SPP1 phage G39P [49], *Bst* DnaI [16, 50–52], and *E. coli* phage T4 gp59 [53] helicase loaders. The DciA helicase loaders are organized around a type II K homology domain (KH) with Lasso elements at either the amino or carboxy terminus of a particular ortholog or both [12, 14, 40, 41, 54].

Cells apply three broad strategies to load hexameric helicases onto nucleic acid substrates: ring-opening, ring-forming, and ring-closing [22, 55, 56] (Supplementary Fig. S1 and Supplementary Information). Although much is known about many bacterial loaders [11, 12, 14, 16, 19, 36, 42–46], little is known about DciA helicase loaders and the mechanisms they implement during helicase loading. DciA orthologs from *Vibrio cholerae* (*Vc*), *Mycobacterium tuberculosis* (*Mt*), and *Caulobacter crescentus* (*Cc*) are all essential proteins [37, 42, 57, 58], and they have been shown to bind to cognate DnaB helicases [12, 14, 42, 57, 58]. The component KH and Lasso domains interact with DnaB [12, 14, 58]. The binding site on DnaB for DciA is proposed to encompass the DH–LH interface [12, 14, 58]. DciA orthologs bind to DNA [11, 58, 59], a feature shared with other bacterial loaders [31, 35, 47, 60]. Suppression of DnaB's ATPase activity is a hallmark of the bacterial helicase loaders [43, 46, 60]; however, *Cc*DciA has been reported to promote ATP hydrolysis [42]. DciA activates cognate DnaB's DNA unwinding activity by mediating assembly on ssDNA, though the underlying mechanisms have yet to be established [40, 41].

To gain insights into the mechanisms operating during the loading of DnaB by the DciA loader and subsequent translocation, we studied the orthologs from *Vibrio cholerae*. The single-particle cryogenic electron microscopy (cryo-EM) structure of the *Vc*DnaB-ssDNA-ATPγS (ATPγS: Adenosine 5'-O-[γ-thio]triphosphate) complex, representing the end state of helicase loading, suggests that cycles of opening and closing of the NTD layer and CTD layer remodeling are significant features in the mechanism of translocation on ssDNA. We suggest that remodeling of the NTD layer and the distinct migration of two subunits to the top of the DnaB spiral, repeated three times, mediates hand-over-hand translocation. Native mass spectrometry (nMS) indicates that *Vc*DnaB is a hexamer, and that the stoichiometry of the *Vc*DnaB–DciA–ssDNA complex is 6:3:1. *Vc*DciA features a KH domain at its amino terminus and a disordered segment (lasso) at its carboxy terminus [12, 40, 41, 54, 58]. Binding experiments demonstrate that the lasso segment accounts for most of the binding energy in its interaction with DnaB. Furthermore, *Vc*DciA binds to DnaB at the interface between the docking helix (DH) and linker helix (LH) on adjacent subunits. *Vc*DciA suppresses the intrinsic ATPase activity of DnaB. We demonstrate that *Vc*DciA loads DnaB onto ssDNA and activates unwinding. Overall, our data suggest that *Vc*DciA is a ring-opening helicase loader.

Materials and methods

Protein biochemistry

Standard techniques [61] were employed to develop the nine proteins utilized in this study. Our research included efforts with full-length forms and designed truncations of DnaB and DciA from *Vibrio cholerae* (Supplementary Fig. S2). The DnaB constructs consisted of the full-length sequence (1-468), the DnaB amino-terminal domain (NTD; 1–170), the DnaB amino-terminal domain fused to the Linker Helix (NTD-LH; 1–208), and the Linker helix fused to the DnaB carboxy-terminal domain (CTD; 208–468). The DciA constructs comprised the complete sequence (1–157), the KH domain (1–98), and the Lasso domains (98–157). The supplementary methods section (Supplementary Methods and Tables S1 and S2) provides full details on plasmid construction, bacterial expression, and protein purification.

Interactions between DnaB and DciA, along with their respective truncations, were investigated by co-lysing bacteria that expressed each protein separately, with only one of the proteins being histidine-tagged. The lysate was passed over Ni-NTA agarose (QIAGEN), washed to remove contaminants, and histidine-tagged proteins were eluted. Interactions were assessed based on how well the untagged protein in the experiment was retained on Ni-NTA agarose (QIAGEN)

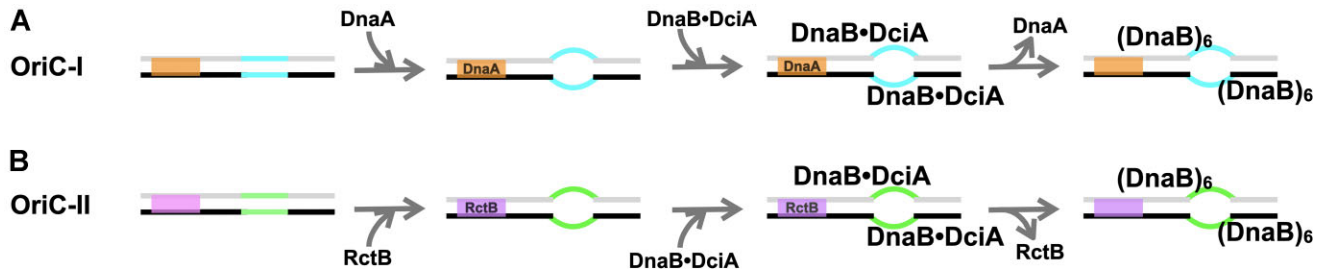

Figure 1. Initiation of DNA Replication in *Vibrio cholerae*. The primary (**A**) and secondary chromosomes (**B**) in *Vibrio cholerae* initiate replication via related but distinct mechanisms. Multiple copies of the replication initiator protein (OriC-I: *Vc*DnaA; OriC-II: *Vc*RctB) recognize sites on dsDNA (OriC-I: orange, OriC-II: purple) and oligomerize into a protein-DNA ensemble. Assembly of the initiator-origin DNA complex promotes the melting of an A-T-rich segment at the origin, termed the DNA unwinding element (DUE, OriC-I: cyan, OriC-II: green). The melted DUE segment provides the sites for the *Vc*DciA loader to load the *Vc*DnaB replicative helicase.

compared to trials where the histidine-tagged protein was excluded. The supplementary methods section provides a more detailed description of the 'pull-down' experiments.

Surface plasmon resonance

Dissociation constants (K_D) were estimated using surface plasmon resonance (SPR) from measurements of the on and off rates between DnaB and DciA. SPR data were acquired using a Biacore X100 instrument (GE Healthcare/Cytiva), and a CM5 sensor chip functionalized with an anti-histidine antibody according to the manufacturer's instructions. All measurements were conducted at 25°C. Since the SPR response is proportional to molecular weight, we chose to immobilize the smaller C-terminal-His-tagged-DciA (MW = 18.4 kDa) while positioning the much larger DnaB (MW = 312.3 kDa) in the mobile phase. DciA was immobilized on the surface of a single channel of the CM5 sensor chip via the interaction between the histidine tag and the anti-histidine antibody. The appropriate ligand density (RL) on the chip was calculated according to the equation: $RL = (\frac{ligand\ MW}{analyte\ MW}) \times R_{max} \times (\frac{1}{S_m})$ where R_{max} is the maximum binding signal, and S_m corresponds to the binding stoichiometry. With the immobilization procedure complete, non-specifically bound proteins were removed by washing with buffer HBS-EP+ (Cytiva) until the resonance signal reached a constant baseline. The reference flow cell provided a control surface for changes in refractive index and non-specific binding. DnaB solution was injected five times at increasing concentrations over the DciA-functionalized sensor surface in a single-cycle kinetics experiment. A long dissociation phase and a single regeneration step followed the last sample injection without regeneration between each sample injection.

The interaction between DnaB and DciA was assumed to display 1:1 kinetics; as such, the measured SPR data should display pseudo-first-order kinetics, which is described by the following rate equation:

$$\frac{d[LA]}{d[t]} = k_a \cdot [L] \cdot [A] - k_d [LA] \quad (1)$$

where k_a is the association rate constant, which refers to the rate of complex formation (units: $M^{-1}s^{-1}$); the dissociation rate constant k_d describes the stability of the complex, i.e. the fraction of complexes that dissociate in the time frame (units: M). [A] represents the analyte concentration; [LA] is the complex concentration measured directly as R in Resonance Units (RU); [L] is the ligand concentration on the surface.

To enable fitting of the SPR data, Equation (1) was modified as follows:

$$\frac{d[R]}{d[t]} = k_a \cdot [C] \cdot [Rmax - R] - k_d [R] \quad (2)$$

where Rmax is the maximum binding capacity, and Rmax-R is the free concentration of the analyte. Rmax and R were extracted from the experimental SPR curves. The fitted data provided estimates for k_d and k_a from which $K_D = k_d/k_a$ was calculated. Experimental binding kinetic data were fit to the '1:1 binding' model implemented in the Biacore X100 Control Software (Cytiva).

nMS

*Vc*DnaB and *Vc*DciA samples for nMS were exchanged into 500 mM ammonium acetate, pH 7.5, and 0.01% Tween-20 (nMS buffer) using a Zeba micro spin desalting column with a molecular cutoff of 40 kDa (ThermoFisher Scientific). Complexes containing DnaB and DciA in the above buffer were mixed in defined molar ratios before nMS measurements. To take data in the presence of nucleotide, ATP and magnesium acetate were added to final concentrations of 10 μM and 0.5 mM, respectively.

The list of DNA molecules used in the nMS study appears in Supplementary Table S2. Lyophilized synthesized ssDNAs (IDT) oligonucleotides were dissolved at 200 μM in HPLC-grade water and diluted to a working concentration of 3–6 μM in the above nMS buffer.

An aliquot (3–5 μL) of the experimental sample was loaded into a gold-coated quartz capillary tip prepared in-house. The sample was then electrosprayed into an Exactive Plus EMR instrument (ThermoFisher Scientific) using a modified static nanospray source [61, 62]. Spectra were continuously recorded from a single capillary loaded with a sample. For analysis of DnaB and DnaB-containing assemblies, the general MS parameters used include spray voltage, 1.2–1.3 kV; capillary temperature, 125–150°C; S-lens RF level, 200; resolving power, 8750 or 17 500 at m/z of 200; AGC target, 1×10^6; number of micro scans, 5; max0imum injection time, 200 ms; in-source dissociation (ISD), 0–10 V; injection flatapole, 8 V; interflatapole, 4 V; bent flatapole, 4 V; high energy collision dissociation (HCD), 200 V; ultrahigh vacuum pressure, 5–7 $\times 10^{-10}$ mbar; total number of scans, 100. For analysis of full-length *Vc*DciA, the MS parameters are simi-

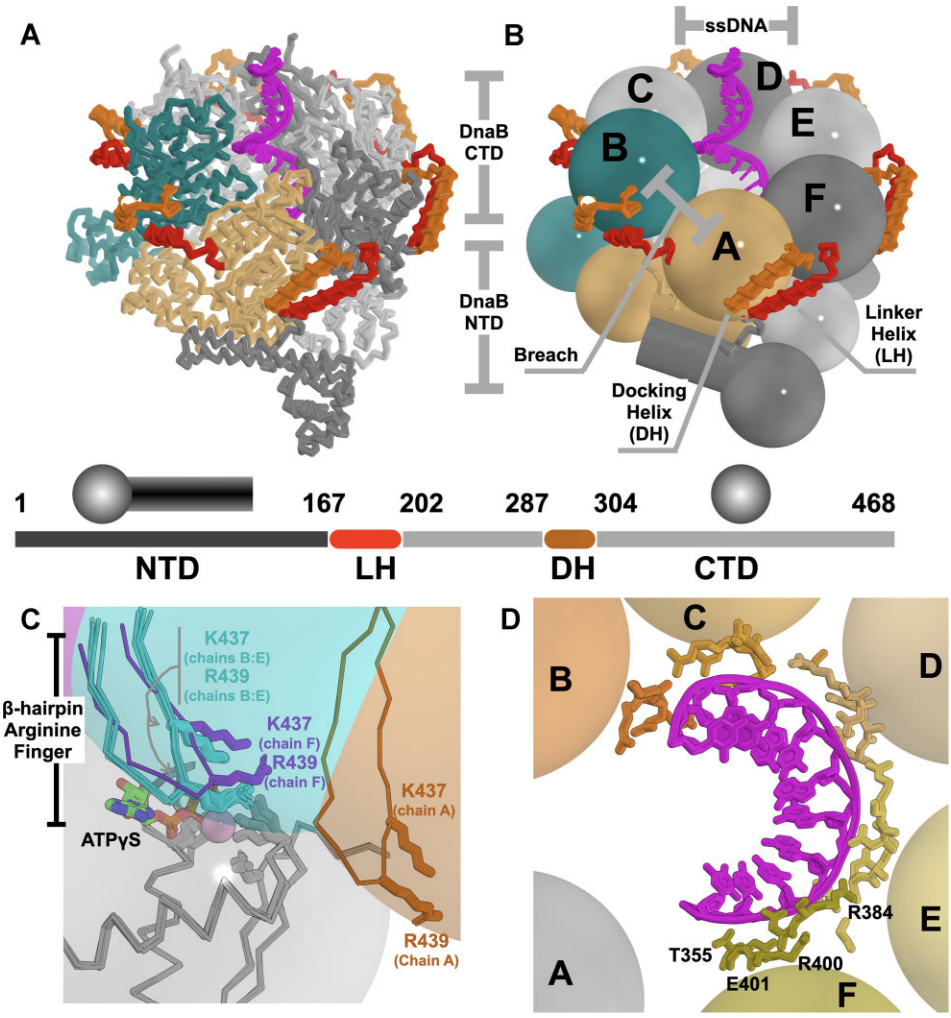

Figure 2. The *Vc*DnaB–ssDNA–ATPγS complex and its interactions with nucleotide and ssDNA. The *Vc*DnaB-ssDNA-ATPγS is drawn in a ribbon representation (**A**) or a schematic using a design language wherein the NTDs are depicted as a mushroom shape and the CTDs as spheres (**B**). In panels A and B, ssDNA, colored magenta, is depicted in both cartoon and stick representations. The breach in the CTD layer is between chain A (light orange) and chain B (deep teal); other DnaB subunits are colored in alternating shades of gray. The Docking Helix (DH) and the Linker Helix (LH) are depicted as cylinders and ribbons colored orange and red, respectively. The primary sequence of *Vc*DnaB is depicted as a bar, with the salient domain boundaries indicated. (**C**) Close-up of the ATP catalytic center at the interface between each pair of DnaB CTDs. ATP is depicted in the stick representation. The six DnaB CTD pairs, depicted here as spheres, are superimposed on the subunit (colored in gray) that harbors the Walker A and B motifs (not indicated). For clarity, only a portion of the superimposed CTD is shown as a ribbon; the gray sphere shows the full extent of the superimposed CTD. Spheres corresponding to the CTDs excluded from the superposition are colored in purple (chain F), cyan (chains B:E), and orange (chain A). The β-hairpin arginine fingers from all six non-superimposed CTDs are shown in the ribbon format. Although excluded from the superposition, the β-hairpin four corresponding to four chains (chains B–E, cyan) superimpose closely. In contrast, chains F (purple) and A (orange) are found ∼3 and ∼19 Å, respectively. (**D**) Schematic representation of the *Vc*DnaB–ssDNA interface. The DnaB CTDs are represented as spheres, labeled by the chain, and colored in shades of yellow/orange, except for chain A, which is colored gray. The ssDNA is depicted in a cartoon and stick representation, colored purple. Additional details on the *Vc*DnaB–ssDNA complex can be found in Supplementary Figs S7, S11, and Supplementary Table S4.

lar as above except for capillary temperature, 100°C ISD, 100 V; injection flatapole, 8 V; interflatapole, 7 V; bent flatapole, 6 V; higher-energy collisional dissociation (HCD), 0 V; ultra-high vacuum pressure, 1.4×10^{-10} mbar. Mass calibration in positive EMR mode was performed using a cesium iodide solution. Raw nMS spectra were visualized using Thermo Xcalibur Qual Browser (version 4.2.47). Data processing and spectra deconvolution was performed using UniDec version 4.2.0 [63, 64] with the following general parameters: background subtraction (if applied), subtract curve, 10; smooth charge distribution, enabled; peak shape function, Gaussian; degree of Softmax distribution (beta parameter): 2–20. PDBO measured all mass spectrometric data in the laboratory of BTC.

FRET-based DNA strand displacement assay

DNA unwinding by *Vc*DnaB and its stimulation by *Vc*DciA were measured using a fluorescence resonance energy transfer (FRET) helicase strand displacement assay adapted from reference [20]. The DNA substrates for the assay FRET-DNA-fork-top-strand, FRET-DNA-fork-bottom-strand, and FRET-DNA-fork-capture-oligo are identical to those described in reference [20]. The top strand is labeled with Cy3 at its 5′ end; the bottom strand is labeled with the BHQ_2 quencher at its 3′ end. The capture oligo is unlabeled (Supplementary Table S2).

Strand displacement was measured by mixing annealed and fluorescence-quenched substrates at a concentration of 100 nM with 200 nM DnaB and DciA concentrations ranging

from 0 to 6400 nM. An excess of the capture oligo (400 nM) was included to prevent the re-annealing of the fork after strand displacement. FRET data were taken at 37°C in the following buffer: 20 mM K-HEPES pH = 7.5, 5 mM Mg acetate, 50 mM K-glutamate, 5% glycerol, and 4 mM dithiothreitol (DTT). Reaction components were mixed into wells (volume: 100 μL/well) of a Corning black plate (p/n: 3880) with 96 half-area clear flat bottom wells. The working concentration of NaCl in the assay is 50 mM. The reaction was initiated by adding 1 mM ATP to each well; the plate was subsequently inserted in a SpectraMax M5 plate reader (Molecular Devices). FRET signals were recorded for 30 min at 37°C. To avoid the crosstalk between Cy3′s closely spaced excitation and emission signals, an excitation wavelength of 520 nm was used; at this wavelength, excitation is reduced to 50% of its maximal value (https://www.thermofisher.com/us/en/home/life-science/cell-analysis/fluorophores/cy3-dye.html); however, this wavelength does not overlap with the fluorescence emission peak, measured at 570 nm. Relative Fluorescence Unit (RFU) data taken in this way were exported for analysis in Microsoft Excel and GraphPad Prism.

FRET-based replicative helicase loading assay

To measure helicase loading by DciA, we adapted the unwinding assay described above; instead of a fork substrate with 5′ and 3′ unpaired segments, we employed substrates that featured single-stranded 'bubbles' (Supplementary Table S2) whose sequences are taken from (#894 and #895, reference: [42]). Bubble substrates favor DnaB assembly on ssDNA instead of threading the free end of ssDNA into the DnaB central chamber. In our first bubble substrate, the top strand was singly labeled at the 5′ end with Cy3, and the bottom strand with the Iowa Black RQ quencher (IDT). To account for the possibility that DnaB helicase could, in principle, be loaded for translocation in either direction, we employed a second substrate wherein fluorophore – quencher pairs were installed at both ends of the 'bubble' (Supplementary Information); such a substrate could inform on the loading and translocation on both strands and in both directions. As with the strand displacement assay, unlabeled capture strands forestalled the re-annealing of the quencher-containing bubble strand. FRET signals from helicase loading were recorded and analyzed as described for the strand displacement assay.

Single particle cryo-EM

Samples for cryo-EM were prepared and imaged, and the images were processed using standard techniques and software [65–68]. Supplementary Methods, Supplementary Figs S3 and S4, and Supplementary Table S3 provide detailed descriptions.

Model building and structure refinement

The DeepEMhancer-sharpened map H (Supplementary Fig. S3) was selected to build a molecular model of the *Vc*DnaB–ssDNA complex. Map H was submitted to ModelAngelo [69] to construct the initial protein and DNA model. The quality of the resulting model was high, despite containing numerous chain breaks. Next, we superimposed the AlphaFold predicted structure of *Vc*DnaB, which has been split into three component domains (*N*-terminal domain (NTD, residues 1:170), Linker Helix (LH, residues 171:211), and C-terminal domain (CTD, residues 212:468)), onto the ModelAngelo output to create a model of hexameric *Vc*DnaB with excellent stereochemistry. The program COOT [70] was used to connect domains belonging to each monomer and to remove the following DnaB residues (chain A, B: 1-21 and 463:468, C-E-F: 1:21 and 464:468, D: 1:22 and 464:468) because of missing map density. Although *Vc*DciA was present in a four-fold excess in our cryo-EM sample, we found no EM density that the *Vc*DnaB model did not explain. As such, we conclude that *Vc*DciA is not present in our reconstruction.

The EM density in map H revealed an 11-mer ssDNA within the internal chamber of DnaB. This was sufficiently resolved to distinguish the DNA backbone from the nucleobases; however, it was not so resolved to permit assigning the nucleotide sequence to the map. In many places, purines could be distinguished from pyrimidines; however, we could not unambiguously position the 60-mer ssDNA in our cryo-EM sample. An 11-mer ssDNA molecule (TCCAGATACAC) was constructed in COOT [70, 71] and placed in density using its 'real space refine' function. In the lower-resolution map E0 (6.24 Å, Supplementary Fig. S3), we observed density extending away from DnaB along the axis where the 11-mer had been constructed. The density quality in this map did not permit the DNA backbone to be distinguished from the nucleobases. However, model building suggested that an additional 11 nucleobases could explain this density. Since this density provided no unique nucleobase information, we built this segment as polyadenine. The extra 11 DNA bases visible in Map E0 were refined in COOT against this map. The complete 22-mer ssDNA was refined against the high-resolution map H.

The *Vc*DnaB-ssDNA-ATPγS model was refined with Phenix [72–79]. We used the 'real_space_refine' protocol, which encompasses global minimization, morphing, NQH flips, and atomic displacement parameters (ADP). The refinement leveraged three rigid bodies (DnaB residues 1:171, 171:211, 212:468, 501 for each chain; ssDNA 1:11), Ramachandran, and secondary structure restraints. Refinement was carried out against the DeepEMhancer-sharpened 3.37 Å density map H. A second round of real-space refinement, encompassing global minimization, ADPs, NQH flips, and Ramachandran and secondary structure restraints, completed the model (Supplementary Table S3). The final model includes Chain A (DnaB residues 22:461), Chain B (DnaB residues 22:462), Chain D (DnaB residues 23:463), Chains C-E-F (DnaB residues 22:463), six ATPγS•Mg^{2+} complexes, one per chain (chains A-B-C-D-E-F residue 501), and ssDNA (chain G, residues 1–22).

Model analysis and visualization

Structural analysis and visualization of the *Vc*DnaB–ssDNA complex were performed in the CCP4 software package [80], Coot [70, 71], the Uppsala software suite [81–84], UCSF-CHIMERA [85], Phenix [72–79], PyMOL [86], Nucplot [87], and as described previously [44]. Distances and angles within and between protein structures were calculated using the PyMol Python scripts titled "pairwise_dist" (https://pymolwiki.org/index.php/Pairwise_distances) and "angle_between_domains" ((https://pymolwiki.org/index.php/Angle_between_domains). Molecular graphics and figures were generated using UCSF-CHIMERA [85] and PYMOL [86]. The software used in this study was sourced from the SBGrid Consortium [88, 89].

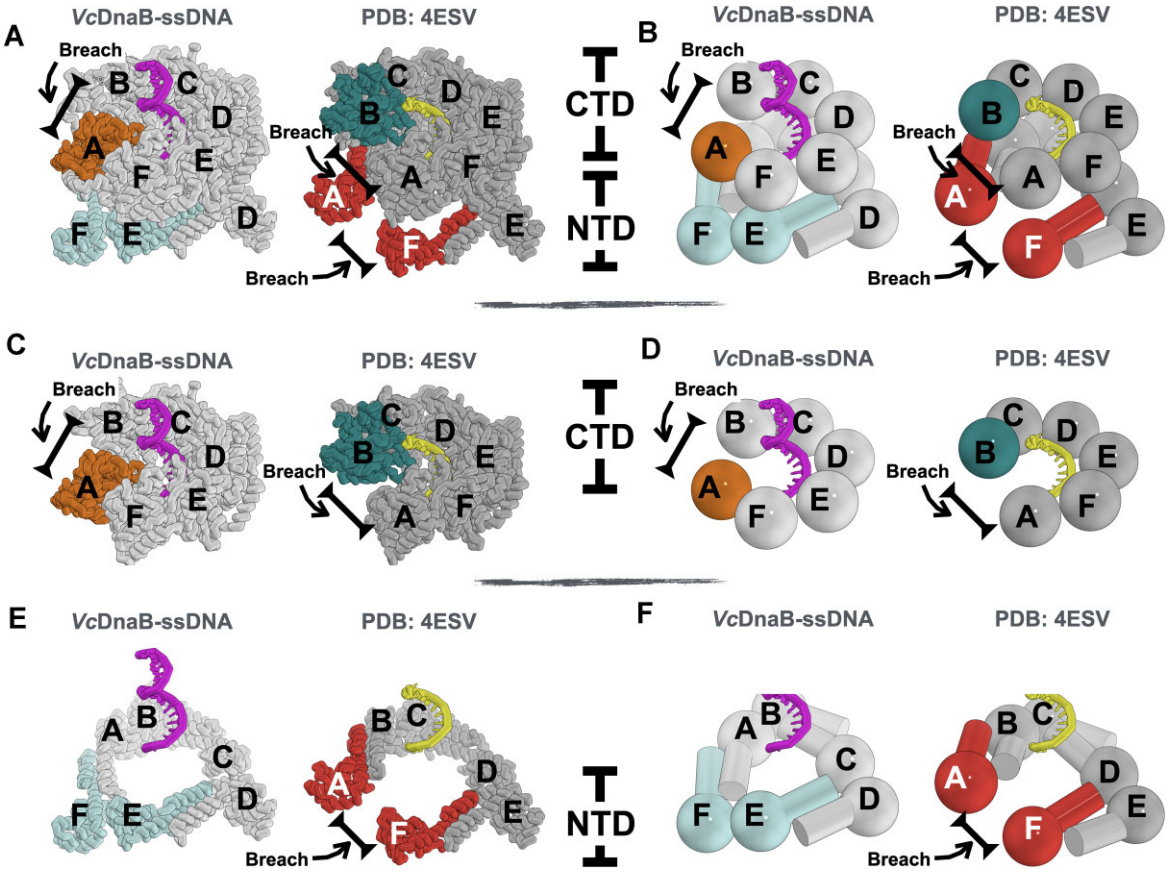

Figure 3. Nucleotide-dependent conformational differences in the *Vc*DnaB–ssDNA–ATPγS and *Bst*GDP•AlF_4 complexes. The two complexes are superimposed in all panels, as described in the main text. For clarity, the two entities have been translated with respect to each other, allowing each to be visible. (**A**) Ribbon representation of both complexes. *Vc*DnaB NTD components chain F and E in the closed planar and triangular configuration are colored in pale cyan. *Bst*-DnaB NTD components chain A and F in the open spiral configuration are colored in red. *Vc*DnaB chain A is colored orange. 4ESV chain B is colored deep teal. The ssDNA in the *Vc* and *Bst* complexes is depicted in both cartoon and stick representations, colored purple and yellow, respectively. All other chains of DnaB are colored in light gray (*Vc*) and dark gray (*Bst*). The breaches in the NTD and CTD layers are indicated. Chains corresponding to the N-terminal domain (NTD) and C-terminal domain (CTD) components are labeled. (**B**) The depiction is identical to that in panel A, except that the NTD and CTD layers are represented using the sphere and mushroom-like shape design language. (**C**) The exact representation as panel A, except that only the CTD layer is shown. (**D**) Identical depiction as panel C except that the DnaB CTD layers are depicted as spheres. (**E**) The exact representation as panel A, except that only the NTD layer is shown. (**F**) Identical depiction as panel E except that the DnaB NTD layers are depicted using mushroom-like shapes.

Results

Cryo-EM structure of *Vc*DnaB bound to ssDNA and ATPγS

To understand the loading of the DnaB helicase by DciA, we applied single-particle cryo-EM to the *Vc*DnaB helicase bound to ATPγS, *Vc*DciA, and ssDNA derived from the *Vc*OriC-I replication origin. In assembling the complex, we relied on results from our nMS study (below). Cryo-EM analysis (Supplementary Methods, Supplementary Figs S3, S4, and Supplementary Table S3) produced a 3.37 Å structure of hexameric *Vc*DnaB bound to ATPγS and complexed to a 22-nucleotide ssDNA molecule (Fig. 2 and Supplementary Figs S5–S8). The resolution of the EM density corresponding to one of the chains (chain A) was lower than that of the other chains. Notwithstanding the fourfold excess in the cryo-EM sample, our maps displayed no density corresponding to the DciA loader. Our *Vc*DnaB–ssDNA complex likely represents the end-state structure after DciA-mediated loading or self-threading.

Compared to the *Bst*–DnaB–ssDNA complex, determined with GDP•AlF_4 (PDB: 4ESV [10]), the ATPγS form of the *Vc*DnaB–ssDNA complex presents a distinct configuration (Fig. 3). Both share the trimer of dimers and pseudo-sixfold architecture of the NTD and CTD tiers. With diameters of ∼55 and ∼25 Å, the NTD and CTD layers in the *Vc*–ATPγS complex are dilated and constricted [8], respectively (Figs 2, 3, and Supplementary Fig. S8A–D). However, the six-chain NTD tier from the *Vc*–ATPγS complex structure adopts a closed triangular planar and symmetric arrangement, resembling the NTD tier from other structures (PDB: 2R5U [90], root mean square deviation (RMSD) = 2.6 Å over 558 Cα atoms; PDB: 7T20 [91], RMSD = 1.5 Å over 825 Cα atoms). This configuration differs from the open spiral in the GDP•AlF_4 form of the *Bst*–DnaB–ssDNA complex [10]. As with other DnaB structures, the *Vc* NTD assembles around weak (head to head) and strong (tail to tail) interfaces, defined by buried surface area [7]; the NTD tier in the *Bst* structure is breached on the weak head-to-head interface. In both nucleotide forms, the constricted CTD tier is arranged as a closed spiral; however, the spirals are distinct (Supplementary Fig. S9). The six DnaB subunits in the *Vc* and *Bst* structures are labeled A-F-E-D-C-B around the spiral; the breach in the CTD tier spiral

lies between chains A and B, which are at the bottom and top of the spiral (as in the pose in Fig. 2A and B), respectively. Five of the six subunits of each structure (PDB: 4ESV: residues 181:441 and chain C, D, E, F, and A on *Vc*DnaB: residues 204:441 and chain B, C, D, E, and F) chains could be superimposed with an RMSD of 1.7 Å (1016 Cα atoms). The most significant difference in CTD configurations is the distinct position occupied by *Vc*DnaB chain A, which maps to chain B in the GDP•AlF4 4ESV structure; we address this change in greater detail below. We also note that in the *Vc* ATPγS complex, chain A is located further away from its neighbors (distances to chain B: ∼39.6 Å, to chain F: ∼34.6 Å) than the average distance separating the remaining four subunits to their neighbors (Chains C, D, E, and F: ∼33.4 Å). By contrast, in the GDP•AlF4 4ESV structure, Chain A is distant from one immediate neighbor (distance between chains B and A: 42.6 Å), while other chains are 32.5 Å from their neighbors. Lastly, in the *Vc*–ATPγS complex, the six Linker Helices (LH) occupy three positions relative to the NTD and CTD. The LH elements of chains B, C, D, and E occupy one position (LH1), with chains F (LH3) and A (LH2) diverging from this position by rotations/displacements of ∼16.5°/∼7.1 and ∼29.6°/12.3 Å, respectively. In the GDP•AlF_4 4ESV complex, the LH elements occupy two positions, one by chains B, C, D, E, and F (LH1) and a second position (LH4) by chain A (Supplementary Fig. S10).

ssDNA in the complex traces a spiral path that passes through the internal chamber of *Vc*DnaB (Fig. 2). Eleven of the 22 ssDNA nucleotides are bound to subunits of the *Vc*DnaB hexamer; the remaining 11 are outside the DnaB perimeter (Supplementary Figs S7 and S11). In contrast to the GDP•AlF_4 4ESV structure, where each subunit contacts ssDNA, only five DnaB subunits in the current *Vc* structure make contacts (less than 4.0 Å); chain A does not contact ssDNA. An inventory of protein-DNA contacts reveals the involvement of seven *Vc*DnaB residues, though not every contact is made by each subunit (Supplementary Table S4).

Six ATPγS/Mg^{2+} complexes are found at composite catalytic centers formed between adjacent *Vc*DnaB subunits, wherein the Walker A/P-loop and Walker B motifs are provided by one subunit and the β-hairpin arginine finger by a second (Fig. 2C and Supplementary Figs S6 and S8E). In four nucleotide sites (chain F-E, E-D, D-C, and C-B), the β-hairpin/arginine finger makes a close approach to nucleotide on a neighboring subunit, with distances between the P-loop lysine (K234) and the arginine (R439) finger residues of ∼11.3 Å. The corresponding distance at the A–F subunit interface is slightly longer (∼11.9 Å), and the arginine finger has shifted by ∼3 Å relative to other subunits. The β-hairpin/arginine finger at the nucleotide site that lines the breach (B-A) exhibits a considerably longer (∼24.5 Å) distance. In the *Bst*GDP•AlF_4 complex, 5/6 sites (Chains A-F, F-E, E-D, D-C, and C-B) feature an average P-loop lysine (K216) to arginine (R420) finger distance of ∼11.4; the chain B-A site, which lines the breach, has a considerably longer distance at ∼32.8 Å.

Taken together, the significant changes between the GDP•AlF_4 and ATPγS forms of DnaB, including distinct NTD configurations, the offset of a single DnaB CTD, and diversity in LH element conformations in sequential subunits around the ring, imply that our structure has captured a distinct intermediate in the translocation reaction.

Remodeling of the NTD and CTD tiers accompanying translocation

To place the distinct ATPγS form of DnaB in the translocation reaction, we compared it to the *Bst*GDP•AlF_4 [10] entity (Fig. 3) and a series of DNA complexes (PDB: 6N7I, 6N7S, 6N7T, and 6N7V) of the DnaB-family helicase Gp4 from phage T7 [24, 29] (Comparisons to other *Vc*DnaB structures appear in the Supplementary Information). Aligning the *Vc* ATPγS and *Bst*GDP•AlF_4 structures by superimposing 5/6 CTDs (RMSD: 1.7 Å, a similar alignment could be obtained by aligning on the ssDNA (RMSD: 0.64 Å) reveals that chain A of the *Vc* ATPγS complex, excluded from the alignment, is displaced by 25 Å and rotated by ∼22° relative to the corresponding subunit in 4ESV (Chain B). Similar displacements and rotations are observed in the HelF subunits of the 6N7T and 6N7V DnaB-family Gp4 helicase structures, resulting in shifts of ∼24 Å and 13° [24, 29]. Furthermore, the DnaB alignment juxtaposes all the components of the NTD layer, except for the chains at the top (4ESV: chain A) and bottom (4ESV: chain F) of the *Bst* spiral. These two chains are offset owing to the distinct planar versus spiral configurations adopted by the NTD tier of the *Vc* ATPγS and *Bst*GDP•AlF_4 complexes. Unexpectedly, the breaches in the two structures do not align (Fig. 3). Instead, they are offset by one subunit.

Given the distinct states captured by each structure, we reasoned that the *Vc* ATPγS structure might precede the transition state *Bst* complex in the DNA translocation reaction coordinate. Ordering the structures in this way specifies a direction for the observed structural changes. Accordingly, the NTD of chain F and chain E in the *Vc* ATPγS complex will transition from the closed triangular planar configuration to the open spiral of the GDP•AlF_4 complex (mapped to 4ESV chains: A and F); concomitantly, the chain A CTD of the *Vc*–ATPγS complex will move upward (as in the pose in Fig. 2A and B) to assume the configuration seen in chain B of 4ESV (Supplementary Movie 1). With the migration of the chain A CTD of the *Vc* ATPγS complex to the position specified in the 4ESV structure, the breach in the CTD spiral moves counterclockwise by one subunit. The LH element moves from the LH3 to the LH4 position in 4ESV chain A. Several lines of evidence in the *Vc* ATPγS complex support the proposal that the chain A CTD migrates (Fig. 3). First, the arginine finger/β-hairpin element on chain F has peeled away by ∼3 Å, relative to its position in chains B, C, D, and E, from the P-loop on chain A (Fig. 2C). Secondly, chain A is farther away from its neighbors than any other DnaB subunit. Third, chain A makes no contact with ssDNA. Lastly, of all the CTDs, the EM density for chain A is the weakest. Together, these findings suggest that the chain A CTD disengages from its CTD neighbors and ssDNA as it prepares to transition. Of course, the chain A CTD remains linked to the DnaB hexamer through its NTD.

Due to the NTD layer's asymmetry, the next subunit's motion, chain F, must follow a different trajectory. We propose that on ATP hydrolysis, chain F, now located at the bottom of the spiral, will also peel away from DNA and migrate upwards to a new binding site on ssDNA. In contrast to the motion of chain A, which results in the opening of the NTD layer, the motion of chain F CTD must be accompanied by the closure of the NTD ring from the open spiral to the closed planar configuration; this motion will also result in the adjustment of the position of the LH element, from the LH3 position to the LH1. Together, these two changes re-establish the NTD

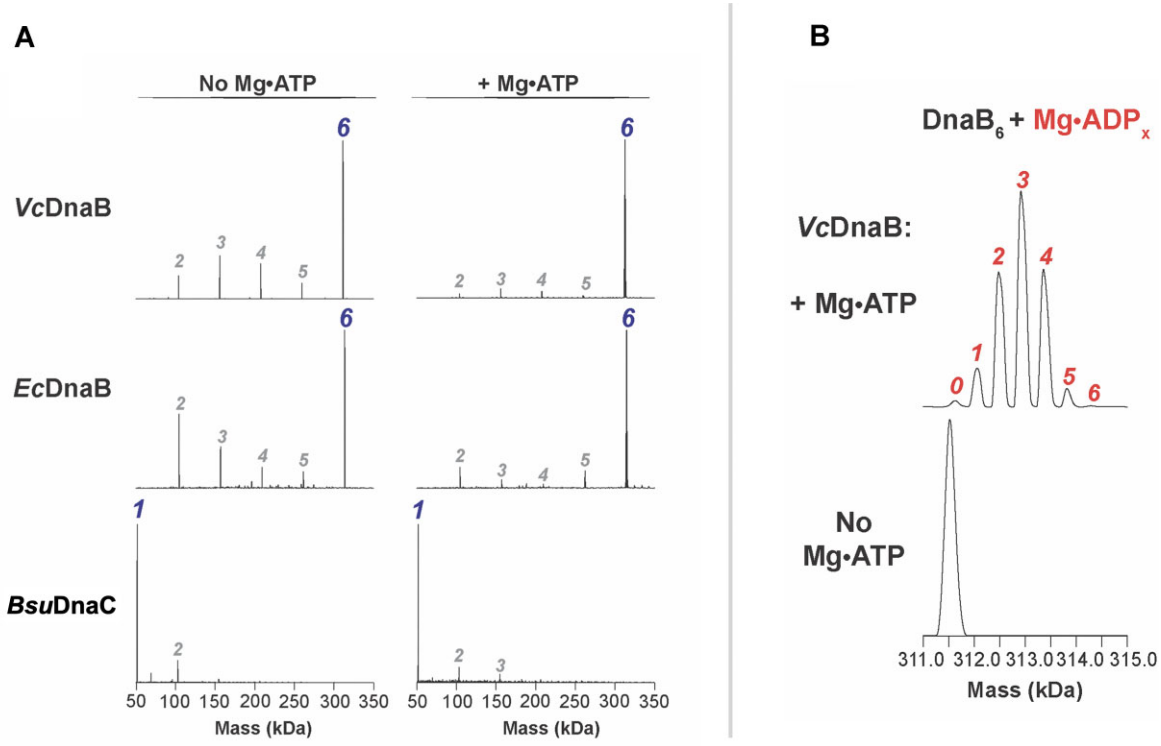

Figure 4. Although highly conserved, certain DnaB helicase orthologs feature distinct oligomeric states. (**A**) Deconvolved nMS spectra of replicative helicases from *V. cholerae* (*Vc*), *E. coli* (Ec), and *B. subtilis* (*Bsu*) with and without Mg•ATP. Unlike the *B. subtilis* ortholog, which is monomeric (with or without ATP), *V. cholerae* and *E. coli* DnaB are hexamers. Each measurement was performed with a monomeric protein concentration of 10 μM. The *Bsu*DnaC sample refers to the DnaB family helicase in *B. subtilis*. (**B**) Close-up of panel A peaks corresponding to the hexameric *Vc*DnaB complex. The average mass difference between adjacent peaks is 444 ± 20 Da; this value more closely matches the mass of ADP (Mass = 427 Da) than ATP (Mass = 507 Da). As such, we suggest that ATP hydrolysis has occurred, resulting in distinct Mg•ADP-occupied states. The numbers in panels A and B refer to the oligomeric state of *Vc*DnaB (A, blue) and of Mg-ADP molecules bound to *Vc*DnaB (B, red). A list of mass assignments of the various nucleotide-bound peaks in panels A and B appears in Supplementary Table S5.

configuration in the *Vc* ATPγS structure. Applying the above to chains E and D first and then to chains C and B allows each DnaB subunit to complete a catalytic cycle of ATP hydrolysis amid translocation on ssDNA. These findings underscore the significance of opening and closing the NTD layer, which has previously been proposed to determine the direction of unwinding [92] during the translocation reaction.

Oligomeric state and stoichiometry of *Vc*DnaB, DciA, and ssDNA complexes

Next, we used high-resolution nMS to determine the oligomeric states and the stoichiometry of complexes in the DnaB-DciA system assembled from purified proteins (Supplementary Fig. S2). We first investigated the oligomeric states of DnaB complexes from *Vc*. To provide context, the hexameric *E. coli* (*Ec*) DnaB [22] and monomeric *B. subtilis* (*Bsu*) DnaB-family species [34] were included. nMS analysis showed that the *Vc*DnaB helicase is hexameric (Fig. 4A and Supplementary Table S5). We observed a sizeable population of lower oligomeric states for *Ec* and *Vc*DnaB ($DnaB_5$, $DnaB_4$, $DnaB_3$, and $DnaB_2$) in samples without Mg•ATP. The addition of a small amount of ATP (10 μM ATP for a 10 μM DnaB monomer sample) before nMS analysis yielded a predominant peak for the hexameric DnaB with minimal subcomplexes (Fig. 4A and Supplementary Table S5), indicating that ATP stabilizes the *Vc*DnaB hexamer as previously suggested for the *E. coli* ortholog ([93], [92]). All subsequent experiments with DnaB-containing samples were supplemented with 10 μM ATP and 0.5 mM magnesium acetate before nMS analysis. Close-up inspection of the nMS spectrum for the *Vc*DnaB sample incubated with Mg•ATP showed a peak distribution corresponding to several Mg•ADP-bound states, indicating ATP binding and hydrolysis (Fig. 4B and Supplementary Table S5).

Next, we examined complexes between *Vc*DnaB, *Vc*DciA, and ssDNA derived from the OriC-I chromosomal origin. Our nMS analysis showed that *Vc*DciA is monomeric (Supplementary Fig. S12). Incubation of 10 μM (as monomer) *Vc*DnaB with 7 μM full-length *Vc*DciA, in the absence of ssDNA, revealed that the DnaB hexamer bound 1–2 copies of DciA, with small amounts of a third copy (Fig. 5A). We attempted to analyze samples with higher relative amounts of DciA (> 10:7 DnaB: DciA) but encountered significant disassembly of *Vc*DnaB complexes with *Vc*DciA upon initiation of electrospray during nMS analysis (Supplementary Fig. S13). Stoichiometries of 6:3 or 6:6 for the *Vc*DnaB–*Vc*DciA complex have been estimated from small-angle X-ray scattering and the X-ray crystal structure [12, 14].

DnaB accepts ssDNA into its central chamber, the basis for the fork DNA unwinding assay [12, 42, 94]. Accordingly, we found that *Vc*DnaB alone could bind OriC-I-derived ssDNA (Fig. 5B). An nMS analysis of a mixture comprising *Vc*DnaB, *Vc*DciA, and the ssDNA showed that up to three copies of *Vc*DciA could be associated with ssDNA-bound DnaB. Interestingly, there is a marked increase in the relative peak inten-

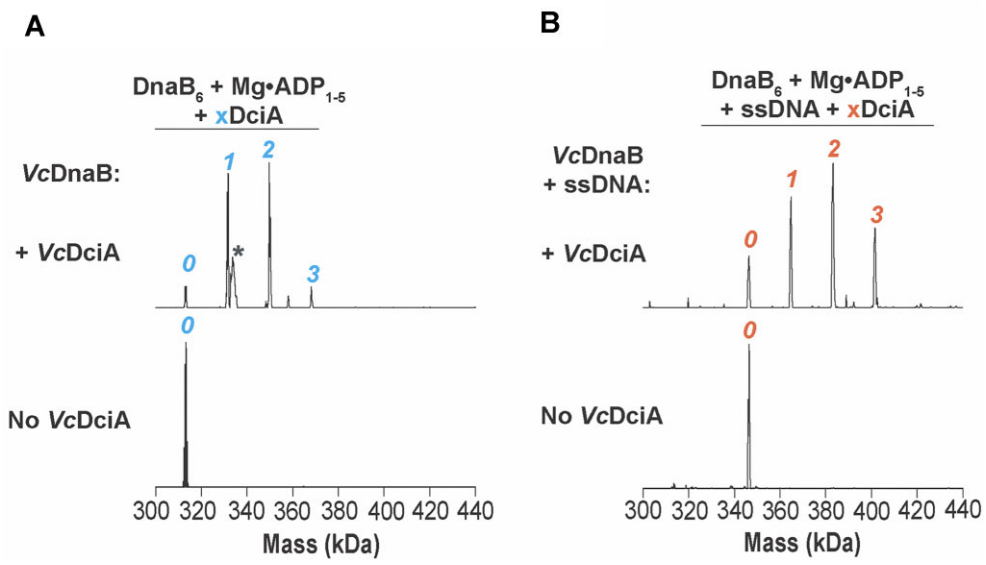

Figure 5. Up to three copies of *Vc*DciA bind to isolated hexameric *Vc*DnaB and *Vc*DnaB complexed to replication origin-derived ssDNA. Deconvolved nMS spectra of 10 μM *Vc*DnaB (measured as the monomer) without and with 7 μM full-length *Vc*DciA (**A**) and in the absence or presence of 3 μM origin-derived ssDNA (O4-*Vc*-F) (**B**). The number of *Vc*DciA molecules observed bound to *Vc*DnaB is indicated in blue (**A**) or red (**B**). The expected masses include $DnaB_6$ = 311.5 kDa, DciA = 18.4 kDa, and ssDNA = 32.5 kDa. The broad peak (*) is from an unknown low-level protein contaminant introduced during or after buffer exchange for this sample. All samples were exchanged into 10 μM ATP, 500 μM magnesium acetate, 500 mM ammonium acetate, and 0.01% Tween-20 before nMS analysis.

sity for the 6:3 DnaB: DciA assembly when ssDNA is bound compared to the ssDNA-free sample, suggesting that ssDNA association promotes the formation or stabilization of this higher-order ensemble.

We also investigated the binding of specific *Vc*DciA domains to *Vc*DnaB. nMS analysis of *Vc*DnaB titrated with increasing concentrations of the lasso domain of DciA showed a progressive increase in the number bound to the DnaB hexamer, with 1–4 copies bound when both proteins are present at equimolar amounts, to 2–6 copies bound at four-fold excess of DciA-Lasso (Supplementary Fig. S14A). In contrast, only one copy of the DciA KH domain was found associated with $DnaB_6$ at ∼10% relative peak intensity even at six-fold molar excess, indicating that the KH domain of DciA weakly binds to DnaB (Supplementary Fig. S14B). Incubation of *Vc*DnaB with the two separate DciA domains at the highest concentrations studied did not change the maximum number of bound copies observed (i.e., one and six for the DciA KH and Lasso domains, respectively, Supplementary Fig. S14B). Contrary to what was observed with DnaB and full-length DciA, no DnaB helicase disassembly was observed during the electrospray nMS analysis when either or both DciA domains were used in excess. Moreover, the distribution of DnaB: DciA-Lasso assemblies did not change (1–4 copies of DciA-Lasso remained bound to $DnaB_6$ at equimolar amounts of both proteins) in the absence or presence of ssDNA (Supplementary Fig. S15).

Our nMS experiments revealed the stoichiometry of the isolated *Vc*DnaB helicase and its complex with DciA and OriC-I-derived ssDNA; both estimates are crucial to deciphering the loading mechanism. The hexameric nature of *Vc*DnaB implies that it is a closed protein ring and that the DciA helicase loader is likely a ring-breaker. The 6:3:1 stoichiometry of the *Vc*DnaB–DciA–ssDNA complex suggests that, although six DciA binding sites may exist on DnaB, only three are utilized; this value will be crucial to understanding how the DnaB–DciA complex interacts with other factors during replication initiation.

*Vc*DciA binds to *Vc*DnaB helicases with high affinity

Next, we employed orthogonal approaches to demonstrate that DciA binds to its cognate DnaB and that DciA likely binds near the DH–LH interface (Fig. 6). First, we conducted NiNTA 'pull-down' experiments to examine the binding between full-length and truncated constructs of DciA and DnaB (Fig. 6A and Supplementary Fig. S16). We find that full-length *Vc*DciA binds to full-length *Vc*DnaB. Moreover, DnaB constructs that span the LH and CTD domains also retain binding to full-length DciA (a shorter construct spanning the CTD could not be expressed). No other DnaB construct (NTD or NTD-LH) showed binding to full-length DciA. Parallel experiments with constituent KH (*Vc*: 1:98) and Lasso domains (*Vc*: 98:157) revealed binding to full-length cognate DnaB, although the *Vc*DciA KH domain bound weakly. No other truncated DnaB construct (NTD or NTD-LH) showed any interaction with either the KH or Lasso domains. These data point to the LH interface as a strong candidate for part of the DciA binding site, with another part comprised of the CTD itself.

We next applied SPR to quantify the interaction between *Vc*DnaB and *Vc*DciA. We immobilized full-length DciA, the isolated KH domain, and the Lasso domain to the SPR chip, measured on- and off-rates for full-length DnaB, and extracted dissociation constants (Fig. 6B, C, and Supplementary Fig. S17). As our pull-down binding experiments anticipated, *Vc*DnaB bound tightly (K_D = 0.58 nM) to full-length *Vc*DciA. We found that the isolated *Vc* Lasso domain bound to DnaB with a K_D of 65 nM, whereas the KH domain exhibited a weaker affinity (K_D = 170 nM) (Supplementary Fig. S17).

Our data reveal that the most significant contacts between DciA and DnaB are located at the LH and CTD domains of DnaB, with the Lasso domain being the primary locus of these contacts. Given that two other loaders, *E. coli* DnaC and phage λP, bind at the DH–LH interface of two adjacent DnaB subunits [19, 43, 44, 48], the finding that the LH constitutes the DciA binding establishes this site as a conserved location of significance for DnaB helicase loading.

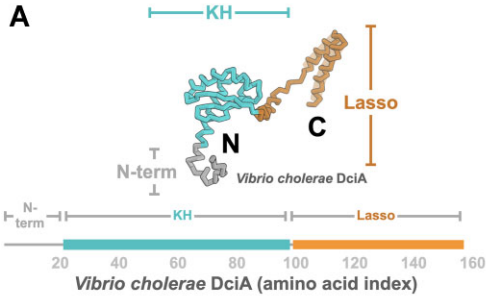

	DnaB Full-length 1:468	DnaB NTD 1:170	DnaB NTD-LH 1:208	DnaB LH-CTD 208:468
DciA Full-length 1:157	Yes	No	No	Yes
DciA KH 1:98	Yes, weakly	No	No	No
DciA Lasso 98:157	Yes	No	No	Yes

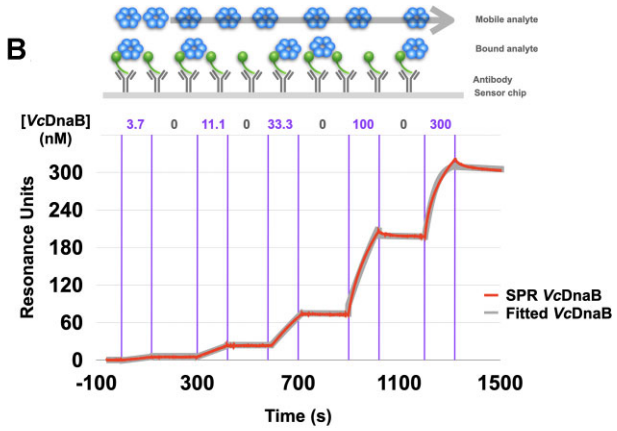

C

	*Vc*DciA Full-length AA: 1-157	*Vc*DciA KH AA: 1-98	*Vc*DciA Lasso AA: 98-157
*Vc*DnaB AA: 1-468	**0.58 nM**	**170 nM**	**65 nM**

Figure 6. The *Vc*DciA loader Binds Tightly to *Vc*DnaB helicase. (**A**) The primary sequence of *Vc*DciA is arranged as a bar, and the locations of the KH and Lasso domains are indicated. The table summarizes the NiNTA 'pull-down' experiments, wherein the green 'yes' and red 'no' indicate that the pull-down assay was scored to report binding or no binding, respectively (Supplementary Fig. S15). (**B**) The dissociation constants (K_D) between DnaB and DciA were evaluated through single-cycle kinetic analyses *via* SPR. On and off rates of full-length DnaB at incremental concentrations (3.7, 11.1, 33.3, 100, and 300 nM) were measured by immobilizing cognate C-term His-tagged full-length *Vc*DciA (C; $K_D = 0.59$ nM; $Chi^2 = 4.33$; $R_{max} = 312.3$) on the SPR sensor chip. A schematic of the SPR experiment accompanies the raw (red) and fitted (gray) SPR curves. The experimental data were analyzed as described in the "Materials and methods" section. The same approach was applied to measure K_Ds for the KH and Lasso constructs (Supplementary Fig. S17). (**C**) The K_D values emerging from the SPR analysis are summarized for the *Vc* system in tabular form.

Suppression of DnaB's ATPase activity by DciA

One of the hallmarks of a bacterial helicase loader is the suppression of ATPase activity of the cognate helicase [43, 46, 60]. To evaluate the effect of *Vc*DciA on the ATPase activity of *Vc*DnaB, we measured the influence of full-length and truncated constructs of DciA against control measurements encompassing wild-type and the Walker B mutant E259A (Fig. 7A). Our preparations of full-length and truncated DciA lacked ATPase activity. Titration of full-length *Vc*DciA revealed potent suppression of *Vc*DnaB's ATPase activity (untagged DnaB: $IC_{50} \approx 26$ nM, NHis-DnaB: $IC_{50} \approx 26$ nM, Fig. 7B). A construct encompassing the *Vc* KH domain (1:98) exhibited an IC_{50} of ~443 nM (Supplementary Fig. S18A); the lower inhibitory constant is congruent with the weak interaction signaled by our nMS study and the NiNTA-based binding studies. Even though we found that the *Vc* Lasso domain (98:157) binds to full-length *Vc*DnaB, titration revealed no effect on *Vc*DnaB's ATPase activity at low DciA concentrations (25–400 nM). However, at very high concentrations (800–6400 nM) of *Vc*DciA, we observed reproducible stimulation (up to 2.8 x at 4800 nM) of DnaB's ATPase activity (Supplementary Fig. S18B).

DciA loads DnaB on physiological DNA bubble substrates

The nMS binding data and DNA unwinding experiments (Supplementary Information and Supplementary Figs S19–S22) suggest that DciA functions as a helicase loader. However, the substrates employed in the above assays (ssDNA, 5′ and 3′ ssDNA tailed fork) do not permit self-threading into DnaB's central chamber to be distinguished from loading/assembly around ssDNA. Physiologically melted DNA by DnaA at a replication origin has no free termini, and, as such, assembly around ssDNA, rather than threading, is expected to be the predominant form of loading *in vivo*.

To distinguish the DciA-mediated assembly of *Vc*DnaB on ssDNA from self-threading, we measured unwinding from a DNA bubble substrate, which features no free ends, unlike a tailed-fork substrate. Our assay employed DNA molecules #894 and #895 previously described in reference [42], which we converted into a FRET-based readout by adding a Cy3 fluorophore at one 5′ end and the Iowa Black RQ quencher at the corresponding 3′ end (Fig. 8). We also measured DnaB loading onto a doubly labeled DNA bubble (Supplementary Information and Figs S23, S24, S25C, and D).

No fluorescence signal was observed when DciA was omitted (Fig. 8, red curve), indicating that the bubble substrate had suppressed the self-threading of ssDNA into DnaB. Titration of full-length *Vc*DciA (0.11–6400 nM) revealed a 10-fold (~15–150) increase in fluorescence at the highest concentration (6400 nM). The increase in fluorescence strictly depended on ATP since the *Vc*DnaB E259A mutant showed no activity (Supplementary Fig. S24). Substitution of the two DciA truncations – the NTD KH and the CTD Lasso – for full-length *Vc*DciA revealed essentially no loading activity (less than 5%) (Supplementary Fig. S25A and B).

To better understand *Vc*DciA's loading activity, we repeated the above titration without *Vc*DnaB. Surprisingly, titration of DciA against the DNA bubble substrate revealed a substantial fluorescence signal (Fig. 8B); these data imply that *Vc*DciA has a previously undiscovered activity: to unwind dsDNA on its own. This activity did not require ATP. The finding that iso-

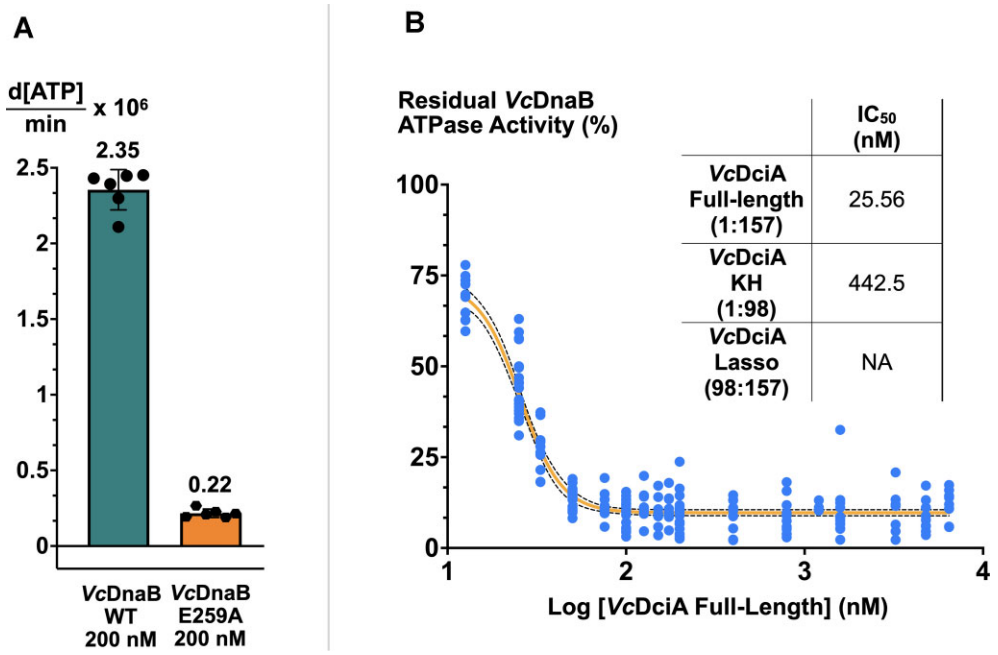

Figure 7. The full-length DciA loader suppresses VcDnaB's ATPase activity. (**A**) ATPase rate of 200 nM wild type (teal) and E259A mutant *Vc*DnaB (orange). The points represent the measured rates; the height of the bar represents the average of the measured points; the vertical bracket visually represents one standard deviation. Each experiment in panel A was performed two times in triplicate. (**A**) The effect of titrating *Vc*DciA (0–6400 nM, log scale) on the residual ATPase activity of *Vc*DnaB (200 nM) is plotted. For each experiment, the residual activity is the quotient of the ATPase rate of a particular DciA concentration and the rate for 0 nM DciA. The blue points represent seven experiments with different batches of *Vc*DnaB and *Vc*DciA measured in triplicate on various days. The light-orange line represents the non-linear fit of the residual activity points (Sigmoidal, 4PL, X is log (concentration) model in Prism. The dotted lines represent the 95% confidence interval. The fit encompassed 210 points, yielding an R^2 value of 0.91 and resulting in an IC_{50} value of 25.56 nM (95% CI, 23.74–26.94 nM). Parallel analysis with the KH domain on four different batches revealed a 16-fold higher IC_{50} of 442.5 nM (R^2 = 0.9693; 95% CI: 380.5–520.0 nM). The Lasso domain was not found to inhibit; however, we observed activation of DnaB's ATPase at very high Lasso concentrations. The inset table summarizes the IC_{50} results. Control measurements with the E259A *Vc*DnaB Walker B mutant exhibited no ATPase activity (panel B, orange).

lated *Vc*DciA produced a fluorescence signal ~66% of that seen in the *Vc*DnaB-DciA titration implies significance, although establishing biological relevance will require further experimentation. DciA's apparent unwinding activity is not observed when the DNA bubble is substituted with the fork substrate (Supplementary Fig. S22), indicating a role for DNA structure in this activity.

We subtracted the two signals to separate the unwinding activities of *Vc*DnaB-DciA and isolated *Vc*DciA (Fig. 8C). The calculated signal from *Vc*DnaB, when acted upon by *Vc*DciA, showed a 25-fold (~5–125 RFU, Fig. 8C) increase in fluorescence at the highest concentration (6400 nM) (Fig. 8D). These data strongly argue that *Vc*DciA is a helicase loader for *Vc*DnaB.

The congruence of the DNA unwinding and helicase loading curves during titration with full-length *Vc*DciA suggests that, to a large degree, helicase loading rather than threading occurs with full-length DciA in both assays (Fig. 8D and Supplementary Fig. S19B). On the other hand, dissimilarity in the curves corresponding to the *Vc*DciA truncations implies that loading is not retained in either construct or that the observed DNA unwinding activity in the truncated constructs may arise solely from self-threading. Our data establish a helicase-loading biochemical activity for the *Vc*DciA protein. Moreover, the finding that loading onto the bubble substrate does not occur without DciA supports a closed protein ring configuration for DnaB, which agrees with our nMS results (Fig. 4A).

Discussion

Our analyses of the bacterial DciA loader and the DnaB helicase from *Vibrio cholerae* shed new light on the underlying helicase-loading and activation pathway (Fig. 9). In bacteria, two copies of the DnaB replicative helicase are assembled onto ssDNA introduced into the replication origin by the DnaA initiator protein. It is now clear that most bacteria lack an ortholog for the well-studied DnaC helicase loader; instead, the DciA helicase loader appears likely to be the predominant loading factor [37, 40, 41]. *Vc* binds to cognate hexameric DnaB with a low nM K_D. The unstructured Lasso segment mediates significant binding energy to the interaction with DnaB, and an essential part of the DciA binding site lies at the nexus of DnaB's DH and LH elements. Prior studies have suggested stoichiometries of 6:3 or 6:6 for the *Vc*DnaB-*Vc*DciA complex, with a binding site located at the DH-LH nexus [12, 14]. We find up to three copies of *Vc*DciA and one copy of replication-origin-derived ssDNA bound to *Vc*DnaB. The stoichiometry of the DnaB-DciA system distinguishes it from the *E. coli* DnaB–DnaC and DnaB•λP complexes, which feature 6:6 and 6:5 stoichiometries, respectively [19, 43, 44, 48]. The unwinding activity of DnaB is significantly stimulated by DciA on fork and replication origin-mimicking DNA bubble substrates. The finding that isolated *Vc*DnaB is a hexamer under physiological concentrations of ATP (Fig. 4A) and exhibits essentially no self-loading on the replication-origin mimicking DNA bubble substrate (Fig. 8) leads us to conclude that DciA is a ring-opening-type helicase loader.

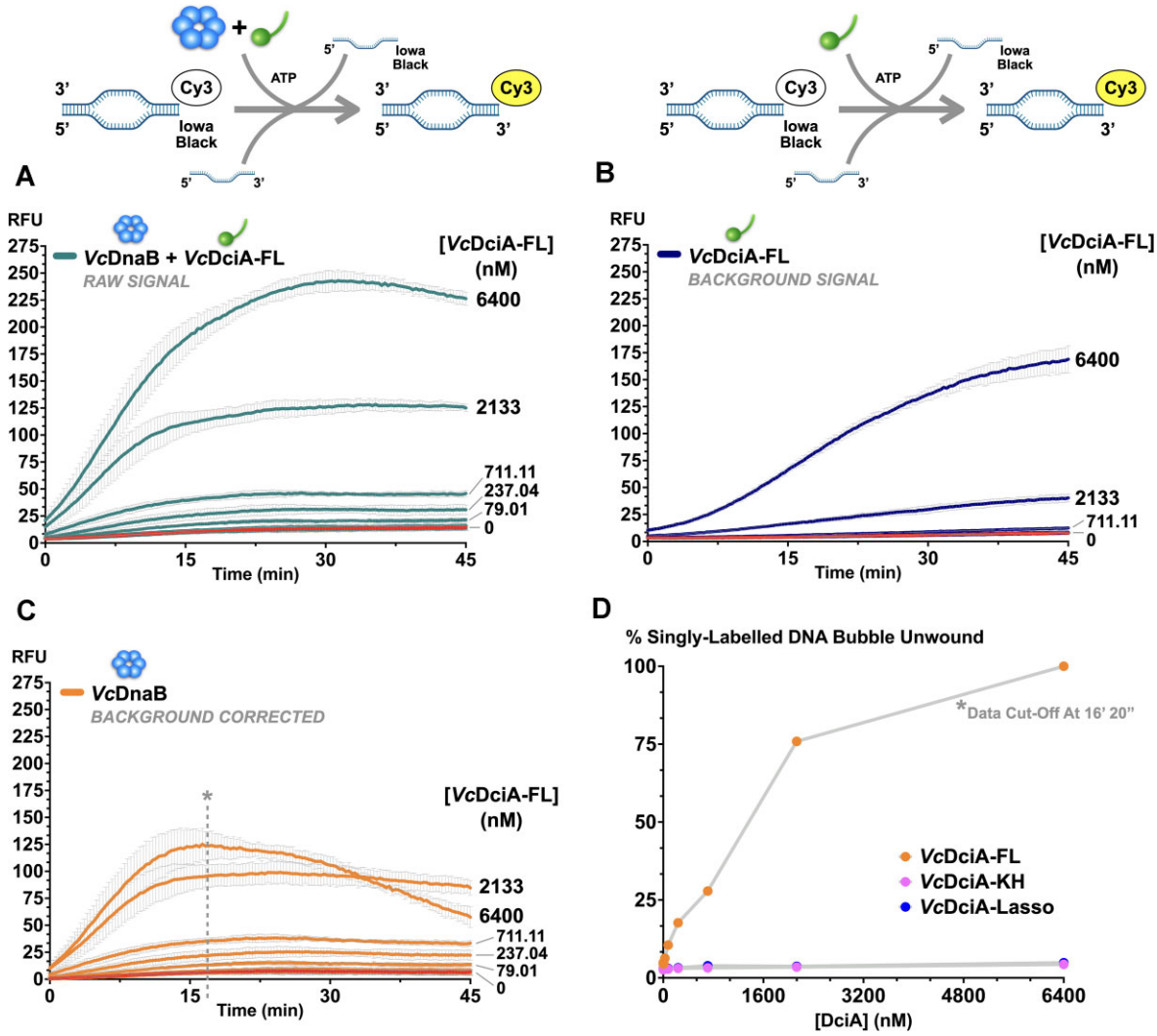

Figure 8. *Vc*DnaB is loaded onto a physiological DNA bubble substrate by the full-length *Vc*DciA loader. Helicase loading was measured using a DNA substrate that mimics unwound DNA at a replication origin, as is diagrammed in the schematic above. (**A**) Loading of full-length *Vc*DnaB by full-length *Vc*DciA. Loading is read out by measuring fluorescence (in RFU) over 45 min at 570 nm from a DNA substrate after it had been unwound by DciA-loaded DnaB; loading relieves the quenching to provide a signal. Data were taken by titrating *Vc*DciA-FL (0.11–6400 nM) against *Vc*DnaB (200 nM). Each labeled curve represents the average of six independent measurements taken from different batches of proteins on different days. The lack of loading activity in the curve that omits *Vc*DciA (red curve) implies that DnaB's self-threading activity has been suppressed with the replication-origin mimicking DNA bubble substrate. The standard deviation of each point is plotted in light gray. (**B**) Same as Panel A except that *Vc*DnaB is omitted. Envisioned as a control, this measurement teaches that *Vc*DciA appears to have the capacity to unwind bubble DNA on its own. (**C**) Point-by-point subtraction of the curves in panels A and B estimates the bubble unwinding signal that arises solely from *Vc*DnaB. The downward phase of the 6400 nM DciA curve after 16 min arises from unwinding rate differences between *Vc*DnaB and *Vc*DciA. These data suggest that *Vc*DciA stimulates the loading of *Vc*DnaB by ~25-fold, within a range of 5–125 RFU. (**D**) The unwinding data in panel C is converted to a percentage unwound by dividing by the maximum RFU point and plotting the resulting values against *Vc*DciA concentration. Parallel measurements reveal that the isolated *Vc*DciA KH and Lasso domains (Supplementary Fig. S25A and B) exhibit little (less than 5%) to no loading activity.

Our structural analysis did not reveal the architecture of the *Vc*DnaB–*Vc*DciA–ssDNA complex. Nevertheless, the structure of the ATPγS form of the DnaB-ssDNA complex provides new insights into the mechanism of translocation. The topologically closed NTD and distinctly configured CTD layers distinguish the ATPγS state from a structure previously determined bound to the transition state ATP analog GDP•AlF_4 [10] and provide a first view of nucleotide-dependent conformational change during ssDNA translocation. Our model for ATP-dependent translocation by DnaB extends the hand-over-hand mechanism [10] by integrating cycles of opening/closing of the NTD layer, reconfiguration of the LH element, and disengagement of individual CTDs from ssDNA and neighboring subunits, followed by migration from the bottom to the top of the DnaB spiral to new ssDNA binding sites. Migration to the top of the spiral is facilitated by the engagement of its β-hairpin arginine finger with a freshly bound ATP by the DnaB subunit that precedes arrival at the top of the spiral. ATP binding also stabilizes contacts to ssDNA. We suggest that translocation encompasses three identical sub-steps. Each sub-step involves migration of the chain A CTD (or chain E or chain C) with the simultaneous opening of the NTD layer into an open spiral, as seen in the GDP•AlF4 4ESV structure. Notably, the open spiral state of the NTD tier would likely influence contacts with the DnaG primase [9, 95], whose complete binding site on DnaB requires a closed NTD tier. In the second

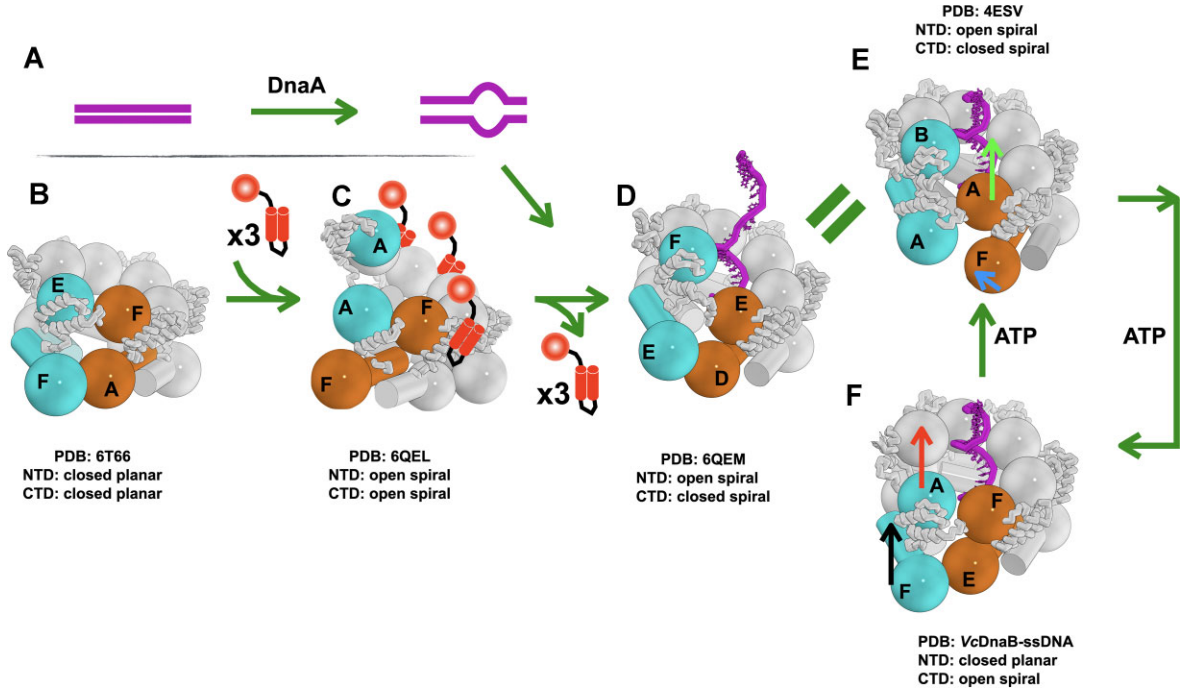

Figure 9. Model for Loading of DnaB by DciA and Translocation of DnaB on ssDNA. (**A**) The DnaA protein binds to the replication origin and promotes melting into a DNA bubble. (**B**) The hexameric closed planar DNA-free *Vc*DnaB (PDB: 6T66 [12]) provides a ground-state model for the loading pathway. (**C**) Our data suggest that up to 3 DciA loaders (red) bind to *Vc*DnaB; we suggest that DnaB adopts an open spiral configuration analogous to that seen with the DnaC/λP complexes [19, 43, 44, 48]. (**D**) Remodeling of this complex accompanies the entry of DnaA-generated ssDNA into the central chamber of DnaB. The current structures suggest that the D and E conformations are identical [19]. We suggest that DnaB populates the two states captured in the GDP•AlF_4 (**E**) and ATPγS (**F**) conformations during translocation. The first translocation step (panel F to panel E) involves opening the NTD tier and the migration of a CTD in the ATPγS complex to its position in the GDP•AlF_4 complex. The ATPγS-chain F NTD shifts (black arrow) in position to the location of the GDP•AlF_4-chain A. Opening of the NTD layer is accompanied by upward migration by 25 Å of the cyan CTD chain A in the ATPγS complex (panel F, red arrow) to the position occupied by chain B in the GDP•AlF_4 complex (panel E); this represents the first translocation step. In the second step (panel E to panel F), the GDP•AlF_4-NTD layer (chain F) returns (blue arrow) to the ATPγS-closed planar configuration (chain E). This change is accompanied by a 25 Å upward migration of the orange CTD chain A in panel E to a new position (chain F) in panel F (green arrow). Repetition of these two steps around the DnaB enables each subunit to translocate. We suggest that the DciA-loaded DnaB-ssDNA complex, which resembles the GDP•AlF_4 conformation, enters this cycle and then transitions to the ATPγS state. The DnaB models in panels B–F are colored in white except for certain blue and orange CTDs and NTDs that line the various breaches, except for the closed planar entity.

step, migration of the next CTD (chain F, chain D, or chain B) in sequence, newly at the bottom of the spiral, is accompanied by the closure of the NTD layer to the triangular planar arrangement seen in the *Vc* ATPγS structure. Our model specifies that two DnaB subunits move in sequence and that this program of motion is repeated thrice around the hexamer.

The precise mechanisms associated with ATP dynamics in ring-shaped oligomeric ATPase are of intense interest [10, 22, 28, 29, 96–100]). Substantial evidence has established sequential ATP hydrolysis during rotary catalysis by the ATP synthase [101, 102]. Within the AAA + family of ATPases, the picture is far less clear, with studies indicating that mechanisms may involve sequential, stochastic, or both processes simultaneously (reviewed in reference [103]) or a concerted mechanism [104]. Our proposal that two adjacent DnaB subunits undergo nucleotide dynamics and motion in sequence is compatible with sequential or stochastic mechanisms, as it disfavors a concerted scheme. Additional studies will be required for a more precise answer.

To link the significant findings of our work in DciA-mediated loading and subsequent translation by DnaB, we looked to another ring-opener, DnaC, to provide models for other steps in the helicase loading pathway (Fig. 9). The configuration of DnaB in the *E. coli* DnaB-DnaC•ssDNA (PDB: 6QEM) complex [19] closely resembles that of the 4ESV GDP•AlF_4 state [10], with a closed spiral CTD and open spiral NTD and contacts to ssDNA by each subunit. DnaB in the 6QEM and 4ESV structures is nearly identical. Thus, on the departure of the loader, DnaB enters the two-subunit motion (Fig. 9E and F) scheme proposed above. Notably, the departure of the DciA loader produces a DnaB configuration after it has taken the first of the two sequential steps described above (Fig. 9D). We suggest that after the eviction of the loader, the subunit at the bottom of the spiral will take the second of these steps to migrate to the top of the spiral (Fig. 9E and F). Repetition of the sequenced motions of two DnaB subunits around the ring accompanies further translocation along ssDNA.

A crystal structure of the 6:6 *Vc*DnaB-*Vc*DciA complex implies two distinct DciA binding modes and a nearly closed planar DnaB ([14] and Supplementary Information and Supplementary Figs S26 and S27). Additional studies will be required to sequence the binding modes in this structure and others that might be present in the helicase loading reaction.

An important unanswered question centers on the mechanism by which DciA is expelled from the DnaB-ssDNA complex. The DnaC [19, 60, 105] and λP [106, 107] systems feature biochemical programs to mediate loader dissociation. Our data reveal a tight interaction between helicase and loader (Fig. 6) that suppresses DnaB's ATPase activity (Fig. 7). Yet,

DciA exhibits a dose-dependent stimulation of DnaB's unwinding activity (Fig. 8 and Supplementary Fig. S19), absent any other factor. These findings suggest that DciA may spontaneously dissociate to relieve inhibition of DnaB's ATPase activity and enable unwinding activities. It is also possible that interactions with other replisome components [25, 105, 108] could contribute to the eviction of DciA. Future studies will have to clarify this question.

Acknowledgements

We thank the Jeruzalmi and Miggiano lab members, the City College biophysics group, the CUNY Advanced Science Research Center, and the New York Structural Biology Center for their scientific and technical advice. We also thank Professor Anuradha Janakiraman for excellent scientific discussions and technical assistance. We are grateful to the reviewers of our manuscript for their careful and insightful critique.

Author contributions: N.Gao, D.M., R.M., and D.J. conceptualized the study. N.Gao designed and prepared all the proteins. N.Gao and D.M. performed the ATPase assays. N.Gao performed the pull-down assays. N.Gouda, S.T., A.M., A.Chowdhury, A.Cerullo, and H.B. assisted with various laboratory experiments. D.M. performed the fluorescence-based DNA unwinding and helicase loading assays. D.M. and C.M. performed the SPR analyses. All nMS analyses were performed by P.D.B.O. in the BTC lab. A.P. and N.Gao acquired the cryo-EM data and performed the initial data analysis. D.M. analyzed the cryo-EM data. D.M. built and analyzed the cryo-EM structure. N.Gao, D.M., R.M., and D.J. drafted the manuscript, working with F.R. and M.R.

Supplementary data

Supplementary data is available at NAR online.

Conflict of interest

The authors have no financial or non-financial conflicts of interest.

Funding

This work was supported by the National Science Foundation (D.J.: MCB 1818255), the Fondazione Cariplo (R.M.: grant #2020–3589), the Italian Ministry of University and Research (R.M.: PRIN 2022, grant #2022LCN738), and the Department of Education (N.Gao: PA200A150068). The nMS work is supported by funding from the National Institutes of Health P41 GM109824 and P41 GM103314 to BTC. Some of this work was performed at the Simons Electron Microscopy Center and National Resource for Automated Molecular Microscopy located at the New York Structural Biology Center, supported by grants from the Simons Foundation (SF349247), NYSTAR, and the NIH National Institute of General Medical Sciences (GM103310) with additional support from Agouron Institute (F00316), NIH (OD019994), and NIH (RR029300). Funding to pay the Open Access publication charges for this article was provided by the National Science Foundation.

Data availability

Coordinates for the EM-derived model of the *Vc*DnaB–ssDNA–ATPγS complex are available from the RCSB Protein Data Bank under accession codes 9DLS. Cryo-EM maps are available from the EMBD under the accession code EMD-46984.

References

1. Parker MW, Botchan MR, Berger JM. Mechanisms and regulation of DNA replication initiation in eukaryotes. *FEMS Microbiol Rev* 2017;**52**:6804–16. https://doi.org/10.1080/10409238.2016.1274717
2. Burgers PMJ, Kunkel TA. Eukaryotic DNA replication fork. *Annu Rev Biochem* 2017;**86**:417–38. https://doi.org/10.1146/annurev-biochem-061516-044709
3. Costa A, Diffley JFX. The initiation of eukaryotic DNA replication. *Annu Rev Biochem* 2022;**91**:107–31. https://doi.org/10.1146/annurev-biochem-072321-110228
4. O'Donnell M, Langston L, Stillman B. Principles and concepts of DNA replication in bacteria, archaea, and eukarya. *Cold Spring Harb Perspect Biol* 2013;**5**:a010108–.
5. Greci MD, Bell SD. Archaeal DNA replication. *Annu Rev Microbiol* 2020;**74**:65–80. https://doi.org/10.1146/annurev-micro-020518-115443
6. Li H, Yao NY, O'Donnell ME. Anatomy of a twin DNA replication factory. *Biochem Soc T* 2020;**48**:2769–78. https://doi.org/10.1042/BST20200640
7. Wang G, Klein MG, Tokonzaba E *et al.* The structure of a DnaB-family replicative helicase and its interactions with primase. *Nat Struct Mol Biol* 2008;**15**:94–100. https://doi.org/10.1038/nsmb1356
8. Strycharska MS, Arias-Palomo E, Lyubimov AY *et al.* Nucleotide and partner-protein control of bacterial replicative helicase structure and function. *Mol Cell* 2013;**52**:844–54. https://doi.org/10.1016/j.molcel.2013.11.016
9. Bailey S, Eliason WK, Steitz TA. Structure of hexameric DnaB helicase and its complex with a domain of DnaG primase. *Science* 2007;**318**:459–63. https://doi.org/10.1126/science.1147353
10. Itsathitphaisarn O, Wing RA, Eliason WK *et al.* The Hexameric Helicase DnaB adopts a nonplanar conformation during translocation. *Cell* 2012;**151**:267–77. https://doi.org/10.1016/j.cell.2012.09.014
11. Cargemel C, Baconnais S, Aumont-Nicaise M *et al.* Structural insights of the DciA helicase loader in its relationship with DNA. *Int J Mol Sci* 2023;**24**:1427. https://doi.org/10.3390/ijms24021427
12. Marsin S, Adam Y, Cargemel C *et al.* Study of the DnaB:dciA interplay reveals insights into the primary mode of loading of the bacterial replicative helicase. *Nucleic Acids Res* 2021;**49**:gkab463. https://doi.org/10.1093/nar/gkab463
13. Cargemel C, Walbott H, Durand D *et al.* The apo-form of the vibrio cholerae replicative helicase DnaB is a labile and inactive planar trimer of dimers. *Febs Lett* 2022;**596**:2031–40. https://doi.org/10.1002/1873-3468.14403
14. Cargemel C, Marsin S, Noiray M *et al.* The LH–DH module of bacterial replicative helicases is the common binding site for DciA and other helicase loaders. *Acta Crystallogr Sect D* 2023;**79**:177–87. https://doi.org/10.1107/S2059798323000281
15. Lo Y-H, Tsai K-L, Sun Y-J *et al.* The crystal structure of a replicative hexameric helicase DnaC and its complex with single-stranded DNA. *Nucleic Acids Res* 2009;**37**:804–14. https://doi.org/10.1093/nar/gkn999
16. Liu B, Eliason WK, Steitz TA. Structure of a helicase-helicase loader complex reveals insights into the mechanism of bacterial primosome assembly. *Nat Commun* 2013;**4**:2495. https://doi.org/10.1038/ncomms3495

17. Bazin A, Cherrier MV, Gutsche I *et al.* Structure and primase-mediated activation of a bacterial dodecameric replicative helicase. *Nucleic Acids Res* 2015;**43**:8564–76. https://doi.org/10.1093/nar/gkv792
18. Nagata K, Okada A, Ohtsuka J *et al.* Crystal structure of the complex of the interaction domains of E. coli DnaB helicase and DnaC helicase loader: structural basis implying a distortion-accumulation mechanism for the DnaB ring opening caused by DnaC binding. *J Biochem* 2019;**5**:a010108.
19. Arias-Palomo E, Puri N, Murray VLO *et al.* Physical basis for the loading of a bacterial replicative helicase onto DNA. *Mol Cell* 2019;**74**:173–84.e4. https://doi.org/10.1016/j.molcel.2019.01.023
20. Arias-Palomo E, O'Shea VL, Hood IV *et al.* The bacterial DnaC helicase loader is a DnaB ring breaker. *Cell* 2013;**153**:438–48. https://doi.org/10.1016/j.cell.2013.03.006
21. O'Donnell ME, Li H. The ring-shaped hexameric helicases that function at DNA replication forks. *Nat Struct Mol Biol* 2018;**25**:122–30. https://doi.org/10.1038/s41594-018-0024-x
22. Fernandez AJ, Berger JM. Mechanisms of hexameric helicases. *Crit Rev Biochem Mol* 2021;**56**:621–39. https://doi.org/10.1080/10409238.2021.1954597
23. Bleichert F, Botchan MR, Berger JM. Mechanisms for initiating cellular DNA replication. *Science* 2017;**355**:eaah6317. https://doi.org/10.1126/science.aah6317
24. Gao Y, Yang W. Different mechanisms for translocation by monomeric and hexameric helicases. *Curr Opin Struct Biol* 2020;**61**:25–32. https://doi.org/10.1016/j.sbi.2019.10.003
25. Spinks RR, Spenkelink LM, Dixon NE *et al.* Single-molecule insights into the dynamics of replicative helicases. *Frontiers Mol Biosci* 2021;**8**:741718. https://doi.org/10.3389/fmolb.2021.741718
26. Perera HM, Behrmann MS, Hoang JM *et al.* Contacts and context that regulate DNA helicase unwinding and replisome progression. *Enzym* 2019;**45**:183–223.
27. Medagli B, Onesti S. DNA helicases and DNA motor proteins. *Adv Exp Med Biol* 2012;**767**:75–95.
28. Hingorani MM, Patel SS. Interactions of bacteriophage T7 DNA primase/helicase protein with single-stranded and double-stranded DNAs. *Biochemistry* 1993;**32**:12478–87. https://doi.org/10.1021/bi00097a028
29. Gao Y, Cui Y, Fox T *et al.* Structures and operating principles of the replisome. *Science* 2019;**363**:eaav7003. https://doi.org/10.1126/science.aav7003
30. Kaguni JM. Molecular Life sciences, an encyclopedic reference. In: *Molecular Life Sciences*. New York, NY, USA: Springer New York, 2014, 1–14.
31. Learn BA, Um SJ, Huang L *et al.* Cryptic single-stranded-DNA binding activities of the phage lambda P and *Escherichia coli* DnaC replication initiation proteins facilitate the transfer of *E. coli* DnaB helicase onto DNA. *Proc Nat Acad Sci USA* 1997;**94**:1154–9. https://doi.org/10.1073/pnas.94.4.1154
32. Bailey S, Sedelnikova SE, Mesa P *et al.* Structural analysis of Bacillus subtilis SPP1 phage helicase loader protein G39P*. *J Biol Chem* 2003;**278**:15304–12. https://doi.org/10.1074/jbc.M209300200
33. Seco EM, Zinder JC, Manhart CM *et al.* Bacteriophage SPP1 DNA replication strategies promote viral and disable host replication in vitro. *Nucleic Acids Res* 2013;**41**:1711–21. https://doi.org/10.1093/nar/gks1290
34. Velten M, McGovern S, Marsin S *et al.* A two-protein strategy for the functional loading of a cellular replicative DNA helicase. *Mol Cell* 2003;**11**:1009–20. https://doi.org/10.1016/S1097-2765(03)00130-8
35. Jones CE, Mueser TC, Dudas KC *et al.* Bacteriophage T4 gene 41 helicase and gene 59 helicase-loading protein: a versatile couple with roles in replication and recombination. *Proc Natl Acad Sci USA* 2001;**98**:8312–8. https://doi.org/10.1073/pnas.121009398
36. Odegrip R, Schoen S, Haggård-Ljungquist E *et al.* The interaction of bacteriophage P2 B protein with *Escherichia coli* DnaB helicase. *J Virol* 2000;**74**:4057–63. https://doi.org/10.1128/JVI.74.9.4057-4063.2000
37. Brézellec P, Vallet-Gely I, Possoz C *et al.* DciA is an ancestral replicative helicase operator essential for bacterial replication initiation. *Nat Commun* 2016;**7**:13271. https://doi.org/10.1038/ncomms13271
38. Brézellec P, Petit M-A, Pasek S *et al.* Domestication of lambda phage genes into a putative third type of replicative helicase matchmaker. *Genome Biol Evol* 2017;**9**:evx111. https://doi.org/10.1093/gbe/evx111
39. Marsin S, Adam Y, Cargemel C *et al.* Study of the DnaB:dciA interplay reveals insights into the primary mode of loading of the bacterial replicative helicase. *Nucleic Acids Res* 2021;**49**:6569–86. https://doi.org/10.1093/nar/gkab463
40. Blaine HC, Burke JT, Ravi J *et al.* DciA helicase operators exhibit diversity across bacterial phyla. *J Bacteriol* 2022;**204**:e00163-22. https://doi.org/10.1128/jb.00163-22
41. Blaine HC, Simmons LA, Stallings CL. Diverse mechanisms of helicase loading during DNA replication initiation in bacteria. *J Bacteriol* 2023;**205**:e00487-22. https://doi.org/10.1128/jb.00487-22
42. Ozaki S, Wang D, Wakasugi Y *et al.* The Caulobacter crescentus DciA promotes chromosome replication through topological loading of the DnaB replicative helicase at replication forks. *Nucleic Acids Res* 2022;**50**:gkac1146. https://doi.org/10.1093/nar/gkac1146
43. Chase J, Berger J, Jeruzalmi D. Convergent evolution in two bacterial replicative helicase loaders. *Trends Biochem Sci* 2022;**47**:620–30. https://doi.org/10.1016/j.tibs.2022.02.005
44. Chase J, Catalano A, Noble AJ *et al.* Mechanisms of opening and closing of the bacterial replicative helicase. *eLife* 2018;**7**:1822. https://doi.org/10.7554/eLife.41140
45. Bell SP, Kaguni JM. Helicase loading at chromosomal origins of replication. *Cold Spring Harb Perspect Biol* 2013;**5**:a010124. https://doi.org/10.1101/cshperspect.a010124
46. Ayora S, Stasiak A, Alonso JC. The Bacillus subtilis bacteriophage SPP1 G39P delivers and activates the G40P DNA helicase upon interacting with the G38P-bound replication origin. *J Mol Biol* 1999;**288**:71–85. https://doi.org/10.1006/jmbi.1999.2662
47. Ioannou C, Schaeffer PM, Dixon NE *et al.* Helicase binding to DnaI exposes a cryptic DNA-binding site during helicase loading in Bacillus subtilis. *Nucleic Acids Res* 2006;**34**:5247–58. https://doi.org/10.1093/nar/gkl690
48. Brown D, Shatarupa A, Olinares PDB *et al.* An autoinhibited conformation of the DnaB-replicative helicase – phage λp helicase loader complex. bioRxiv, https://doi.org/10.1101/2022.12.30.522210, 9 November 2024, preprint: not peer reviewed.
49. AlphaFold-Protein-Structure-Database Inhibitor_G39P domain-containing protein. https://alphafold.ebi.ac.uk/entry/A0A0M0X576
50. Loscha KV, Jaudzems K, Ioannou C *et al.* A novel zinc-binding fold in the helicase interaction domain of the Bacillus subtilis DnaI helicase loader. *Nucleic Acids Res* 2009;**37**:2395–404. https://doi.org/10.1093/nar/gkp092
51. Tsai K-L, Lo Y-H, Sun Y-J *et al.* Molecular interplay between the replicative helicase DnaC and its loader protein DnaI from geobacillus kaustophilus. *J Mol Biol* 2009;**393**:1056–69. https://doi.org/10.1016/j.jmb.2009.09.002
52. AlphaFoldProteinStructureDatabase Bacillus subtilis Primosomal protein DnaI. https://alphafold.ebi.ac.uk/entry/P06567.
53. Mueser TC, Jones CE, Nossal NG *et al.* Bacteriophage T4 gene 59 helicase assembly protein binds replication fork DNA. The 1.45 Å resolution crystal structure reveals a novel α-helical two-domain fold. *J Mol Biol* 2000;**296**:597–612. https://doi.org/10.1006/jmbi.1999.3438

54. Chan-Yao-Chong M, Marsin S, Quevillon-Cheruel S *et al.* Structural ensemble and biological activity of DciA intrinsically disordered region. *J Struct Biol* 2020;**212**:107573. https://doi.org/10.1016/j.jsb.2020.107573
55. O'Shea VL, Berger JM. Loading strategies of ring-shaped nucleic acid translocases and helicases. *Curr Opin Struct Biol* 2014;**25**:16–24. https://doi.org/10.1016/j.sbi.2013.11.006
56. Davey MJ, O'Donnell M. Replicative helicase loaders: ring breakers and ring makers. *Curr Biol* 2003;**13**:R594–6. https://doi.org/10.1016/S0960-9822(03)00523-2
57. Chao MC, Pritchard JR, Zhang YJ *et al.* High-resolution definition of the vibrio cholerae essential gene set with hidden Markov model–based analyses of transposon-insertion sequencing data. *Nucleic Acids Res* 2013;**41**:9033–48. https://doi.org/10.1093/nar/gkt654
58. Mann KM, Huang DL, Hooppaw AJ *et al.* Rv0004 is a new essential member of the mycobacterial DNA replication machinery. *PLoS Genet* 2017;**13**:e1007115. https://doi.org/10.1371/journal.pgen.1007115
59. Quevillon-Cheruel S, Marsin S, Jeannin S *et al.* Dcia, the bacterial replicative helicase loader, is a DNA condenser. 2024, https://doi.org/10.2139/ssrn.4880687
60. Davey MJ, Fang L, McInerney P *et al.* The DnaC helicase loader is a dual ATP/ADP switch protein. *EMBO J* 2002;**21**:3148–59. https://doi.org/10.1093/emboj/cdf308
61. Olinares PDB, Kang JY, Llewellyn E *et al.* Native mass spectrometry-based screening for optimal sample preparation in single-particle cryo-EM. *Structure* 2021;**29**:186–95. https://doi.org/10.1016/j.str.2020.11.001
62. Olinares PDB, Chait BT. The eukaryotic RNA exosome, methods and protocols. *Methods Mol Biol* 2019;**2062**:357–82.
63. Marty MT, Baldwin AJ, Marklund EG *et al.* Bayesian deconvolution of mass and ion mobility spectra: from binary interactions to polydisperse ensembles. *Anal Chem* 2015;**87**:4370–6. https://doi.org/10.1021/acs.analchem.5b00140
64. Reid DJ, Diesing JM, Miller MA *et al.* MetaUniDec: high-throughput deconvolution of native mass spectra. *J Am Soc Mass Spectrom* 2019;**30**:118–27. https://doi.org/10.1007/s13361-018-1951-9
65. de la Cruz MJ, Eng ET. Scaling up cryo-EM for biology and chemistry: the journey from niche technology to mainstream method. *Structure* 2023;**31**:1487–98. https://doi.org/10.1016/j.str.2023.09.009
66. Saibil HR. Cryo-EM in molecular and cellular biology. *Mol Cell* 2022;**82**:274–84. https://doi.org/10.1016/j.molcel.2021.12.016
67. Guaita M, Watters SC, Loerch S. Recent advances and current trends in cryo-electron microscopy. *Curr Opin Struct Biol* 2022;**77**:102484. https://doi.org/10.1016/j.sbi.2022.102484
68. Chari A, Stark H. Prospects and limitations of high-resolution single-particle cryo-electron microscopy. *Annu Rev Biophys* 2023;**52**:391–411. https://doi.org/10.1146/annurev-biophys-111622-091300
69. Jamali K, Käll L, Zhang R *et al.* Automated model building and protein identification in cryo-EM maps. *Nature* 2024;**628**:450–7. https://doi.org/10.1038/s41586-024-07215-4
70. Emsley P, Cowtan K. Coot: model-building tools for molecular graphics. *Acta Crystallogr D Biol Crystallogr* 2004;**60**:2126–32. https://doi.org/10.1107/S0907444904019158
71. Brown A, Long F, Nicholls RA *et al.* Tools for macromolecular model building and refinement into electron cryo-microscopy reconstructions. *Acta Crystallogr D Biol Crystallogr* 2015;**71**:136–53. https://doi.org/10.1107/S1399004714021683
72. Liebschner D, Afonine PV, Baker ML *et al.* Macromolecular structure determination using X-rays, neutrons and electrons: recent developments in Phenix. *Acta Crystallogr Sect D: Struct Biol* 2019;**75**:861–77. https://doi.org/10.1107/S2059798319011471
73. Williams CJ, Headd JJ, Moriarty NW *et al.* . MolProbity: more and better reference data for improved all-atom structure validation. *Protein Sci* 2018;**27**:293–315. https://doi.org/10.1002/pro.3330
74. Echols N, Moriarty NW, Klei HE *et al.* Automating crystallographic structure solution and refinement of protein-ligand complexes. *Acta Crystallogr D Biol Crystallogr* 2014;**70**:144–54. https://doi.org/10.1107/S139900471302748X
75. Zwart PH, Afonine PV, Grosse-Kunstleve RW *et al.* Automated structure solution with the PHENIX suite. *Methods Mol Biol* 2008;**426**:419–35.
76. Afonine PV, Poon BK, Read RJ *et al.* Real-space refinement in PHENIX for cryo-EM and crystallography. *Acta Crystallogr Sect D* 2018;**74**:531–44. https://doi.org/10.1107/S2059798318006551
77. Terwilliger TC, Read RJ, Adams PD *et al.* Model morphing and sequence assignment after molecular replacement. *Acta Crystallogr Sect D: Biol Crystallogr* 2013;**69**:2244–50. https://doi.org/10.1107/S0907444913017770
78. Afonine PV, Grosse-Kunstleve RW, Echols N *et al.* Towards automated crystallographic structure refinement with phenix.Refine. *Acta Crystallogr D Biol Crystallogr* 2012;**68**:352–67. https://doi.org/10.1107/S0907444912001308
79. Adams PD, Afonine PV, Bunkóczi G *et al.* PHENIX: a comprehensive Python-based system for macromolecular structure solution. *Acta Crystallogr D Biol Crystallogr* 2010;**66**:213–21. https://doi.org/10.1107/S0907444909052925
80. Winn MD, Ballard CC, Cowtan KD *et al.* Overview of the CCP4 suite and current developments. *Acta Crystallogr D Biol Crystallogr* 2011;**67**:235–42. https://doi.org/10.1107/S0907444910045749
81. Kleywegt G, Zou J, Kjeldgaard M *et al.* In:Rossmann MG, Himmel D, Arnold E (eds.), *International Tables for Crystallography*, Vol. F, 2001, 353–56.
82. Sierk M, Kleywegt G. Deja Vu all over again: finding and analyzing protein structure similarities. *Structure (London, England : 1993)* 2004;**12**:2103–11.
83. Kleywegt GJ. Quality control and validation. *Methods Mol Biol* 2007;**364**:255–72.
84. Kleywegt G, Jones T. Model building and refinement practice. *Macromol Crystallogr Pt A* 1997;**277**:208–30.
85. Pettersen EF, Goddard TD, Huang CC *et al.* UCSF Chimera–a visualization system for exploratory research and analysis. *J Comput Chem* 2004;**25**:1605–12. https://doi.org/10.1002/jcc.20084
86. Schrodinger-LLC. The PyMOL Molecular Graphics System, Version 3.0, LLC. 2024.
87. Luscombe NM, Laskowski RA, Thornton JM. NUCPLOT: a program to generate schematic diagrams of protein-nucleic acid interactions. *Nucleic Acids Res* 1997;**25**:4940–5. https://doi.org/10.1093/nar/25.24.4940
88. Morin A, Eisenbraun B, Key J *et al.* Collaboration gets the most out of software. *eLife* 2013;**2**:e01456. https://doi.org/10.7554/eLife.01456
89. Herre C, Ho A, Eisenbraun B *et al.* Introduction of the capsules environment to support further growth of the SBGrid structural biology software collection. *Acta Crystallogr Sect D* 2024;**80**:439–50. https://doi.org/10.1107/S2059798324004881
90. Biswas T, Tsodikov OV. Hexameric ring structure of the N-terminal domain of mycobacterium tuberculosis DnaB helicase. *FEBS J* 2008;**275**:3064–71. https://doi.org/10.1111/j.1742-4658.2008.06460.x
91. Oakley AJ, Xu ZQ. *E. coli* DnaB bound to ssDNA and AMPPNP. 2022. https://doi.org/10.2210/pdb7t20/pdb
92. Günther E, Mikolajczyk M, Schuster H. Stabilization by ATP and ADP of *Escherichia coli* dnaB protein activity. *J Biol Chem* 1981;**256**:11970–3. https://doi.org/10.1016/S0021-9258(18)43215-2
93. Nakayama N, Arai N, Kaziro Y *et al.* Structural and functional studies of the dnaB protein using limited proteolysis. Characterization of domains for DNA-dependent ATP hydrolysis

and for protein association in the primosome. *J Biol Chem* 1984;**259**:88–96. https://doi.org/10.1016/S0021-9258(17)43625-8
94. Kaplan DL, Steitz TA. DnaB from Thermus aquaticus unwinds forked duplex DNA with an asymmetric tail length dependence*. *J Biol Chem* 1999;**274**:6889–97. https://doi.org/10.1074/jbc.274.11.6889
95. Oakley AJ, Xu ZQ. *E. coli* DnaB bound to three DnaG C-terminal domains, ssDNA. ADP and AlF4. 2023. https://doi.org/10.2210/pdb7t22/pdb
96. Schlierf M, Wang G, Chen XS *et al.* Hexameric helicase G40P unwinds DNA in single base pair steps. *eLife* 2019;**8**:e42001. https://doi.org/10.7554/eLife.42001
97. Notarnicola SM, Richardson CC. The nucleotide binding site of the helicase/primase of bacteriophage T7. Interaction of mutant and wild-type proteins. *J Biol Chem* 1993;**268**:27198–207. https://doi.org/10.1016/S0021-9258(19)74238-0
98. Patel SS, Hingorani MM, Ng WM. The K318A mutant of bacteriophage T7 DNA primase-helicase protein is deficient in helicase but not primase activity and inhibits primase-helicase protein wild-type activities by heterooligomer formation. *Biochemistry* 1994;**33**:7857–68. https://doi.org/10.1021/bi00191a013
99. Crampton DJ, Mukherjee S, Richardson CC. DNA-induced switch from independent to sequential dTTP hydrolysis in the bacteriophage T7 DNA helicase. *Mol Cell* 2006;**21**:165–74. https://doi.org/10.1016/j.molcel.2005.11.027
100. Crampton DJ, Guo S, Johnson DE *et al.* The arginine finger of bacteriophage T7 gene 4 helicase: role in energy coupling. *Proc Natl Acad Sci USA* 2004;**101**:4373–8. https://doi.org/10.1073/pnas.0400968101
101. Walker JE. The ATP synthase: the understood, the uncertain and the unknown. *Biochem Soc Trans* 2013;**41**:1–16. https://doi.org/10.1042/BST20110773
102. Noji H, Ueno H, McMillan DGG. Catalytic robustness and torque generation of the F1-ATPase. *Biophys Rev* 2017;**9**:103–18. https://doi.org/10.1007/s12551-017-0262-x
103. Khan YA, White KI, Brunger AT. The AAA+ superfamily: a review of the structural and mechanistic principles of these molecular machines. *Crit Rev Biochem Mol Biol* 2022;**57**:156–87. https://doi.org/10.1080/10409238.2021.1979460
104. Pan Y, Zhan J, Jiang Y *et al.* A concerted ATPase cycle of the protein transporter AAA-ATPase Bcs1. *Nat Commun* 2023;**14**:6369. https://doi.org/10.1038/s41467-023-41806-5
105. Makowska-Grzyska M, Kaguni JM. Primase directs the release of DnaC from DnaB. *Mol Cell* 2010;**37**:90–101. https://doi.org/10.1016/j.molcel.2009.12.031
106. Polissi A, Goffin L, Georgopoulos C. The *Escherichia coli* heat shock response and bacteriophage lambda development. *FEMS Microbiol Rev* 1995;**17**:159–69. https://doi.org/10.1111/j.1574-6976.1995.tb00198.x
107. Zylicz M. The *Escherichia coli* chaperones involved in DNA replication. *Philos Trans R Soc Lond Ser B: Biol Sci* 1993;**339**:271–8.
108. Spinks RR, Spenkelink LM, Stratmann SA *et al.* DnaB helicase dynamics in bacterial DNA replication resolved by single-molecule studies. *Nucleic Acids Res* 2021;**49**:gkab493. https://doi.org/10.1093/nar/gkab493

Received: October 2, 2024. **Revised:** May 24, 2025. **Editorial Decision:** May 27, 2025. **Accepted:** June 27, 2025